Petroleum Science 19 (2022) 2046–2063

Contents lists available at ScienceDirect

Petroleum Science

journal homepage: www.keaipublishing.com/en/journals/petroleum-science

Original Paper

Elastic direct envelope inversion based on wave mode decomposition for multi-parameter reconstruction of strong-scattering media

Pan Zhang [a, *], Ru-Shan Wu [b], Li-Guo Han [a, **], Yong Hu [c]

[a] College of Geo-exploration Science and Technology, Jilin University, Changchun 130026, Jilin, China
[b] Modeling and Imaging Laboratory, Earth & Planetary Science, University of California at Santa Cruz, Santa Cruz, California, 95064, USA
[c] School of Resources and Geosciences, China University of Mining and Technology, Xuzhou 221008, Jiangsu, China

ARTICLE INFO

Article history:
Received 2 August 2021
Received in revised form
9 March 2022
Accepted 13 May 2022
Available online 18 May 2022

Edited by Jie Hao

Keywords:
Direct envelope inversion
Full waveform inversion
Elastic wave
Strong-scattering media
Multi-parameter

ABSTRACT

The parameter reconstruction of strong-scattering media is a challenge for conventional full waveform inversion (FWI). Direct envelope inversion (DEI) is an effective method for large-scale and strong-scattering structures imaging without the need of low-frequency seismic data. However, the current DEI methods are all based on the acoustic approximation. Whereas, in real cases, seismic records are the combined effects of the subsurface multi-parameters. Therefore, the study of DEI in elastic media is necessary for the accurate inversion of strong-scattering structures, such as salt domes. In this paper, we propose an elastic direct envelope inversion (EDEI) method based on wave mode decomposition. We define the objective function of EDEI using multi-component seismic data and derive its gradient formulation. To reduce the coupling effects of multi-parameters, we introduce the wave mode decomposition method into the gradient calculation of EDEI. The update of Vp is primarily the contributions of decomposed P-waves. Two approaches on Vs gradient calculation are proposed, i.e. using the petrophysical relation and wave mode decomposition method. Finally, we test the proposed method on a layered salt model and the SEG/EAGE salt model. The results show that the proposed EDEI method can reconstruct reliable large-scale Vp and Vs models of strong-scattering salt structures. The successive elastic FWI can obtain high-precision inversion results of the strong-scattering salt model. The proposed method also has a good anti-noise performance in the moderate noise level.

1. Introduction

Full waveform inversion (FWI) is a high-accuracy seismic velocity imaging method. Different from conventional travel time tomography method, it simultaneously utilizes the travel-time, amplitude and phase information of the observed seismic waveforms (Tarantola, 1984; Virieux and Operto, 2009; Zhang et al., 2021). In recent years, people try to use FWI to build high-precision parameter models of the strong-scattering media, such as salt domes, encountered in real exploration (Ravaut et al., 2008; Lewis et al., 2012; Vigh et al., 2019). The high-accuracy model building of strong-scattering media can improve the imaging quality of strong scatters and its shielding areas. However, as the conventional FWI method is based on the Born approximation (Tarantola, 1984), it is difficult to reconstruct the large-scale and strong-scattering structures in the absence of low-frequency seismic data.

To reconstruct the strong-scattering media using the FWI workflow, the earliest proposed method is the Laplace domain waveform inversion method (Shin and Cha, 2008, 2009). The Laplace transform of wavefield can be used to invert the large-scale structures of the strong-scattering salt bodies in the absence of low-frequency observed data components. Lewis et al. (2012) introduce the level-set approach into the FWI workflow to invert the large-scale and strong-scattering salt geometry. This approach is then developed by many researchers, who extended the level-set FWI to 3D and elastic media (Guo and de Hoop, 2013; Lewis and Vigh, 2016; Wu and Dorn, 2018). FWI with total variation constraint can also help to reconstruct the sharp boundaries and the internal velocity of the salt bodies (Esser et al., 2015). Other

* Corresponding author.
** Corresponding author.
E-mail addresses: zhangpan@jlu.edu.cn (P. Zhang), hanliguo@jlu.edu.cn (L.-G. Han).

https://doi.org/10.1016/j.petsci.2022.05.007

researchers further modify the algorithm of total variation constraint FWI to enhance the quality of strong-scattering salt reconstruction (Esser et al., 2016; Peters and Herrmann, 2017; Yong et al., 2018). Some researchers also try to reconstruct the velocity of strong scatters using the deep learning method. Yang and Ma (2019), and Zhang and Lin (2020) predict the shape of strong-scattering salt structures directly from the original seismic data using the deep convolutional neural network. Gao et al. (2020) adopt the deep autoencoder convolutional neural network to reduce the model parameters and then build the long-wavelength velocity of the strong-scattering salt bodies using the stochastic FWI method. There are also some researches reconstructing the strong scatters by compensating the losing long-wavelength information using some special low-wavenumber retrieving based FWI methods (Wang et al., 2019; Chen and Chen, 2019).

Direct envelope inversion (DEI) is also an effective method for large-scale and strong-scattering velocity reconstruction without the need of low-frequency seismic data and any prior information, and it has relatively high calculation efficiency (Wu and Chen, 2017, 2018; Chen et al., 2019). Different from the conventional envelope inversion method (Chi et al., 2014; Wu et al., 2014; Zhang et al., 2019; Liu et al., 2020), the DEI method avoids the use of the chain rule during the gradient derivation. With the help of the direct envelope Fréchet derivative, the low-frequency envelope residual can be mapped directly to the large-scale and strong velocity perturbations. Chen et al. (2018a) introduce the wavefield decomposition method into DEI and propose a reflection DEI method, which can enhance the inversion quality of the subsalt areas. Zhang et al. (2018) derive a new expression of the envelope data based on the modulation signal model and mitigate the source wavelet dependence of the DEI method. Chen et al. (2018b) add polarity information of the envelope data into DEI process, which can further improve the accuracy of strong-scattering salt and subsalt velocity reconstruction. Hu et al. (2019) integrate the envelope and instantaneous phase information in time-frequency domain to conduct DEI and effectively enhance the inversion result of the salt and subsalt area. Luo et al. (2020) propose an angle-domain DEI method which can invert both the velocity and density of the strong-scattering salt model under the acoustic approximation. Chen et al. (2020) extend the idea of DEI and reconstruct full-band seismic data and high-accuracy salt velocity model with the help of signed envelope information. Luo et al. (2021) conducted some tests using envelope Fréchet derivative in elastic FWI, but the decoupling of multiparameter effects needs further study. In real cases, seismic waves can generate strong converted waves at strong velocity contrast interfaces (Rivera et al., 2019). Therefore, the study of multi-parameter reconstruction of strong-scattering media and the extension of DEI to elastic media are very necessary.

In this paper, we propose an elastic direct envelope inversion (EDEI) method based on wave mode decomposition. Firstly, we define the objective function of EDEI and derive its gradient formulation. Then we provide the calculation approaches of the elastic envelope field and introduce the wave mode decomposition method into the calculation of the Vp and Vs update. Finally, we test the proposed method on a layered salt model and the SEG/EAGE salt model.

2. Review of acoustic full waveform inversion, conventional envelope inversion and direct envelope inversion

2.1. Acoustic full waveform inversion (FWI)

The objective function of conventional FWI in acoustic case can be written as (Tarantola, 1984)

$$\sigma_1 = \frac{1}{2}\sum_{sr}\int_0^T \left[d_{\mathrm{syn}}(t) - d_{\mathrm{obs}}(t)\right]^2 \mathrm{d}t, \tag{1}$$

where d_{syn} and d_{obs} denote the synthetic and observed data, respectively; sr denotes all the source and receiver position; t denotes time; T denotes total recording time length.

The derivative of σ_1 with respect to velocity can be calculated as

$$\frac{\partial \sigma_1}{\partial v} = \sum_{sr}\int_0^T \left[d_{\mathrm{syn}}(t) - d_{\mathrm{obs}}(t)\right] \frac{\partial d_{\mathrm{syn}}(t)}{\partial v}\mathrm{d}t, \tag{2}$$

where $\frac{\partial d_{\mathrm{syn}}(t)}{\partial v}$ is the sensitivity kernel (the Fréchet derivative) of the acoustic FWI. The direct calculation of the Fréchet derivative is always unbearable, so the adjoint state method is proposed to primarily reduce computation, which requires only one additional forward modeling (Plessix, 2006; Wang et al., 2019).

2.2. Conventional envelope inversion (EI)

The problem of FWI is that it may suffer the famous "cycle-skipping" problem if seismic data lacks low-frequency information since low-frequency data always corresponds to the long-wavelength components of the subsurface media (Zhang et al., 2017, 2020; Yao et al., 2020). To overcome the problem caused by low-frequency absence, Wu et al. (2014) propose to take full advantage of the ultra-low frequency information of the envelope data, which is proved to contain the intrinsic long-wavelength responses of the subsurface media. The objective function of the conventional EI can be written as (Chi et al., 2014; Wu et al., 2014)

$$\sigma_2 = \frac{1}{2}\sum_{sr}\int_0^T \left[E_{\mathrm{syn}}(t) - E_{\mathrm{obs}}(t)\right]^2 \mathrm{d}t, \tag{3}$$

where $E_{\mathrm{syn}}(t)$ and $E_{\mathrm{obs}}(t)$ denote the synthetic and observed envelope data, respectively. We can also use the n-th power of the envelope data to form the objective function.

The derivative of σ_2 with respect to velocity can be written as (Wu et al., 2014)

$$\frac{\partial \sigma_2}{\partial v} = \sum_{sr}\int_0^T \left[\frac{\Delta E d_{\mathrm{syn}}}{E_{\mathrm{syn}}} - \mathrm{H}\left\{\frac{\Delta E d^{\mathrm{H}}_{\mathrm{syn}}}{E_{\mathrm{syn}}}\right\}\right] \frac{\partial d_{\mathrm{syn}}(t)}{\partial v}\mathrm{d}t, \tag{4}$$

where ΔE is the envelope data residual, $\mathrm{H}\{\cdot\}$ denotes Hilbert transform, $d^{\mathrm{H}}_{\mathrm{syn}}$ denotes the Hilbert transform of the synthetic data. The derivation of Eq. (4) uses the chain rule, so it has the same Fréchet derivative with FWI.

2.3. Direct envelope inversion (DEI)

As we know, the conventional FWI theory is based on the weak scattering approximation, which requires small-scale and weak parameter perturbation (Wu and Zheng, 2014). Pratt et al. (1998) pointed out that the virtual sources will be highly local, approximating point sources for the point collocation scheme, which means we ignore the mutual interaction of parameters. From the derivation of the adjoint-state method from the perturbation theory (Plessix, 2006), we can clearly see that by only considering the first order Fréchet derivative, the simple expression of the gradient can be easily obtained. In Born approximation, high-order terms in

the Born series are neglected, which means we ignore interactions between different parameter perturbations (multiple scattering), leading to a single scattering approximation (linear approximation, small-scale and weak perturbation approximation). For strong and large volume perturbations, the interactions between perturbations are not negligible, so that the linear Fréchet derivative will produce large errors in predicting the model perturbations (Wu and Zheng, 2014; Wu, 2020).

In the study of this paper, we mainly pay attention to the inversion of complex media with large salt structures. It is explained by Wu (2020) that "in large strong-contrast media, such as salt structures, the strong reflection signals are from boundary scattering", and this "strong-contrast and large-body scattering" can be treated as strong-scattering. In our studies, we pay attention to both large scale and strong contrast scattering, which is the "strong scattering" case in this paper. In general, we assume we only know the background parameter distributions at the beginning of inversion. Therefore, in strong scattering media inversion, the most important thing is to handle large-scale and strong parameter perturbations. The waveform Fréchet derivative will have problems when dealing with the strong-scattering cases since it neglects the high-order terms of the nonlinear partial derivative (Wu and Zheng, 2014; Wu and Chen, 2018; Zhang et al., 2018). To overcome this problem using the ultra-low frequency information contains in the envelope data, the direct envelope Fréchet derivative and the direct envelope inversion is proposed based on the energy scattering theory (Wu and Chen, 2017, 2018; Wu, 1985). The objective function of the acoustic DEI is

$$\sigma_3 = \frac{1}{2}\sum_{sr}\int_0^T \left[E_{\mathrm{syn}}(t) - E_{\mathrm{obs}}(t)\right]^2 \mathrm{d}t, \tag{5}$$

where $E_{\mathrm{syn}}(t)$ and $E_{\mathrm{obs}}(t)$ denote the synthetic and observed envelope data, respectively; sr denotes all the source and receiver position; t denotes time; T denotes total recording time length. The derivative of σ_3 with respect to velocity v is

$$\frac{\partial \sigma_3}{\partial v} = \sum_{sr}\int_0^T \left[E_{\mathrm{syn}}(t) - E_{\mathrm{obs}}(t)\right] \frac{\partial E_{\mathrm{syn}}(t)}{\partial v}\mathrm{d}t, \tag{6}$$

where $E_{\mathrm{syn}}(t) - E_{\mathrm{obs}}(t)$ denotes envelope data residual, which is the adjoint source of DEI; $\frac{\partial E_{\mathrm{syn}}(t)}{\partial v}$ denotes the direct envelope sensitivity kernel (the direct envelope Fréchet derivative). Eq. (6) can be written in a matrix-vector form as

$$\frac{\partial \sigma_3}{\partial \mathbf{v}} = \left(\frac{\partial \mathbf{E}_{\mathrm{syn}}}{\partial \mathbf{v}}\right)^T \left(\mathbf{E}_{\mathrm{syn}} - \mathbf{E}_{\mathrm{obs}}\right), \tag{7}$$

where $()^T$ denotes transpose operator. The Fréchet derivative of acoustic DEI is defined as (Wu and Chen, 2018)

$$\mathbf{F}_E = \frac{\partial \mathbf{E}_{\mathrm{syn}}}{\partial \mathbf{v}} = \mathbf{G}_{\mathrm{e}}\mathbf{Q}_{\mathrm{e}}, \tag{8}$$

where $\mathbf{G}_{\mathrm{e}}$ is the envelope Green's operator, and $\mathbf{Q}_{\mathrm{e}}$ is the envelope virtual source operator. For strong-scattering case, the virtual source operator is (Wu and Chen, 2018)

$$Q_{\mathrm{e}}(x, x', t) = \frac{1}{v_0(x')} g_{\mathrm{e}}(x', t; x_s)\delta(x - x'), \tag{9}$$

where $v_0(x')$ denotes background velocity, g_{e} denotes the envelope Green's operator. In the DEI method, the chain rule is not used, so the envelope data residual is directly mapped to the strong-scattering velocity perturbation. Therefore, the ultra-low frequency information contained in the envelope data residual can be directly used to reconstruct the large-scale components of the velocity perturbation (Wu, 2020).

The current DEI methods are all based on acoustic media. We can reconstruct reliable Vp of the subsurface media using the recorded P-wave data. However, in real cases, seismic records are the combined effects of multi-parameters, so there will be both P-waves and S-waves in the observed data. Since seismic waves always generate strong converted waves at strong contrast interfaces, it is necessary to consider elastic parameters in the strong-scattering media inversion. Fig. 1 shows a comparison of seismic records in the acoustic and elastic strong-scattering cases. Fig. 1a is the pressure data recorded in acoustic media. Fig. 1b is the recorded z-component displacement in elastic media. We can see that the information in the elastic records is much more abundant than that in the acoustic records. We conduct wave mode decomposition during the forward modeling on elastic media and obtain the decomposed P-wave and S-wave records of z-component displacement, which are shown in Fig. 1c and d, respectively. The decoupling method is shown in the later section 3.2. We can see that Fig. 1c is similar to Fig. 1a in waveform shape, but there are converted P-waves recorded in Fig. 1c, such as the waveform denoted by red arrow. Since we use a P-wave source for forward modeling, the S-waves recorded in Fig. 1d are all converted S-waves, which are not appeared in Fig. 1a. Therefore, to adapt the condition in real cases, it is necessary to consider the elastic parameters in the strong-scattering structures inversion.

3. Elastic direct envelope inversion (EDEI) based on wave mode decomposition

3.1. The objective function and the gradient formulation

To consider the converted wave information during the inversion process and reconstruct the multiparameter structures of the subsurface media, elastic full waveform inversion (EFWI) was proposed (Tarantola, 1986; Mora, 1987). Different from acoustic FWI, the EFWI construct the objective function using multicomponent seismic data and can simultaneously invert high-precision λ, μ and ρ. The gradient of EFWI can also be calculated using the adjoint-state method (Plessix, 2006). The gradient formula of Vp and Vs can be derived from the gradient of λ and μ using the chain rule. As the development of computing power, the research on methodology and application of EFWI has greatly increased in recent years (Oh et al., 2018; Wu et al., 2021). Some strategies were proposed to improve the robustness of the EFWI process, such as source-independent approach (Zhang et al., 2016), wave mode decomposition strategy (Ren and Liu, 2016), regularization algorithm (Zhang et al., 2018), local cross-correlation method (Zhang and Alkhalifah, 2019), etc. The EFWI method also has the problem of initial model dependence. Similar with acoustic FWI, if seismic data lacks low-frequency information, it is difficult for EFWI to build high-quality strong-scattering structures. Based on the idea of EFWI, we can extend the acoustic DEI method to elastic media. The objective function for the EDEI can be defined as

$$\sigma_4 = \frac{1}{2}\sum_{sr}\int_0^T \left[E^i_{\mathrm{syn}}(t) - E^i_{\mathrm{obs}}(t)\right]^2 \mathrm{d}t, \tag{10}$$

where $E^i_{\mathrm{syn}}(t)$ and $E^i_{\mathrm{obs}}(t)$ denote the i-th component of the

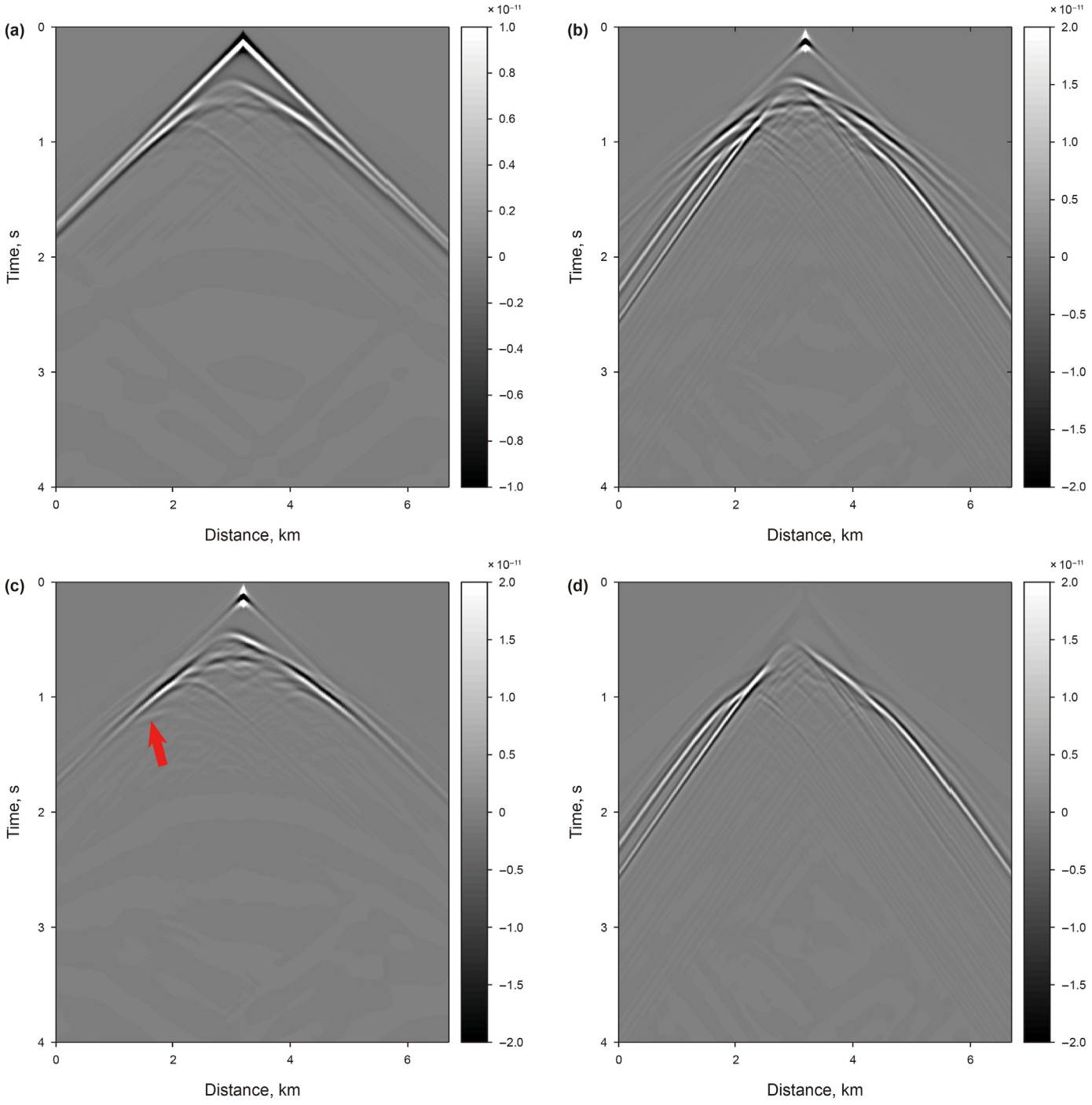

Fig. 1. Comparison of seismic records in the acoustic and elastic strong-scattering cases. (a) is the seismic records in the acoustic case; (b) is the z-component seismic records in the elastic case; (c) is the decomposed z-component P-wave records; (d) is the decomposed z-component S-wave records.

synthetic and observed envelope data, respectively; *sr* denotes all the source and receiver position; t denotes time; T denotes total recording time length. The derivative of σ_4 to the elastic parameter m is

$$\frac{\partial \sigma_4}{\partial m} = \sum_{sr} \int_0^T \left[E^i_{\mathrm{syn}}(t) - E^i_{\mathrm{obs}}(t) \right] \frac{\partial E^i_{\mathrm{syn}}}{\partial m} \mathrm{d}t, \tag{11}$$

where m denotes the Lame constant λ and μ, $\frac{\partial E^i_{\mathrm{syn}}}{\partial m}$ denotes the direct envelope Fréchet derivative of the EDEI, which maps the elastic parameter perturbations directly to the multi-component elastic envelope data perturbations. The establishment of EDEI theory is more complicated than in acoustic medium. As the first step to promote the further development of EDEI method, we try to achieve EDEI from the perspective of wavefield decomposition. Detailed derivation and implementation about this idea will be discussed in the subsequent sections.

3.2. Elastic wave mode decomposition and envelope field calculation

Parameter coupling is a common problem for multi-parameter inversion. Since seismic waves may generate strong converted waves in the strong-scattering media, the multi-parameter coupling effects are especially serious in these cases. In the EFWI, an efficient parameter decoupling method is to combine the EFWI workflow with the wave mode decomposition method based on the radiation pattern analysis of scattering wavefields (Ren and Liu, 2016; Wang and Cheng, 2017; Qu et al., 2018). To enhance the decoupling effects of EDEI, we propose to introduce the wave mode decomposition method into the EDEI.

According to the Helmholtz theorem, the displacement vector of the P- and S-wave in the heterogeneous isotropic media can be calculated by (Tang and McMechan, 2018)

$$\frac{\partial^2 \mathbf{u}_\mathrm{p}}{\partial t^2} = \frac{1}{\rho}\{\nabla[(\lambda+2\mu)\nabla\cdot\mathbf{u}]\}, \tag{12}$$

$$\frac{\partial^2 \mathbf{u}_\mathrm{s}}{\partial t^2} = -\frac{1}{\rho}[\nabla\times(\mu\nabla\times\mathbf{u})]. \tag{13}$$

where $\mathbf{u}_\mathrm{p}$ denotes the displacement vector of P-waves, $\mathbf{u}_\mathrm{s}$ denotes the displacement vector of S-waves, $\mathbf{u}$ denotes the displacement vector of recorded elastic waves, ∇ denotes gradient operator, $\nabla\cdot$ denotes divergence operator, $\nabla\times$ denotes rotation operator, and ρ denotes density.

To facilitate the calculation, the equivalent form of Eqs. (12) and (13) expressed using stress components can be written as

$$\boldsymbol{\sigma}^\mathrm{p} = \begin{bmatrix} \sigma^\mathrm{p}_{xx} & \sigma^\mathrm{p}_{xz} \\ \sigma^\mathrm{p}_{zx} & \sigma^\mathrm{p}_{zz} \end{bmatrix} = (\lambda+2\mu)\begin{bmatrix} \left(\frac{\partial u_x}{\partial x}+\frac{\partial u_z}{\partial z}\right) & 0 \\ 0 & \left(\frac{\partial u_x}{\partial x}+\frac{\partial u_z}{\partial z}\right) \end{bmatrix}, \tag{14}$$

$$\boldsymbol{\sigma}^\mathrm{s} = \begin{bmatrix} \sigma^\mathrm{s}_{xx} & \sigma^\mathrm{s}_{xz} \\ \sigma^\mathrm{s}_{zx} & \sigma^\mathrm{s}_{zz} \end{bmatrix} = \mu\begin{bmatrix} 0 & \left(\frac{\partial u_z}{\partial x}-\frac{\partial u_x}{\partial z}\right) \\ \left(\frac{\partial u_x}{\partial z}-\frac{\partial u_z}{\partial x}\right) & 0 \end{bmatrix}, \tag{15}$$

where σ denotes stress components; the subscripts x and z denote horizontal and vertical direction, respectively; the superscripts p and s denote P-wave and S-wave components, respectively.

Fig. 2 shows a test of elastic wave mode decomposition. The Vp and Vs models are shown in Fig. 2a and b, respectively. The velocity contrast between the high-velocity layer and the background is 2000 m/s for Vp and 1330 m/s for Vs. The thickness of the high-velocity layer is 380 m. We use a P-wave source for forward modeling. The source wavelet is a Ricker wavelet with a dominant frequency of 12 Hz. The snapshot of z-component displacement at 600 ms is shown in Fig. 2c. The decomposed z-component P and S snapshots are shown in Fig. 2d and e, respectively. We can see that the P- and S-waves are separated well. From Fig. 2e, we know that there are strong converted S-waves, which is also the typical characteristics of the strong-scattering cases.

After obtaining the P- and S-wave field, we can calculate the corresponding envelope field. As P- and S-wave can be studied independently in the homogeneous isotropic media, we firstly demonstrate the envelope field calculation for the P- and S- wave in this simple medium in the following.

Based on the theory of elastic dynamics, the wave equation can be expressed in the vector form as

$$(\lambda+2\mu)\nabla(\nabla\cdot\mathbf{u}) - \mu\nabla\times\nabla\times\mathbf{u} + \rho\mathbf{F} = \rho\frac{\partial^2\mathbf{u}}{\partial t^2}, \tag{16}$$

where $\mathbf{u}$ denotes the displacement vector, $\mathbf{F}$ is the force term. According to the Helmholtz theorem, the displacement $\mathbf{u}$ can be written as

$$\mathbf{u} = \mathbf{u}_\mathrm{p} + \mathbf{u}_\mathrm{s} = \nabla\varphi + \nabla\times\boldsymbol{\psi}, \tag{17}$$

where φ and $\boldsymbol{\psi}$ are the scalar potential and vector potential of $\mathbf{u}$, respectively; $\mathbf{u}_\mathrm{p}$ and $\mathbf{u}_\mathrm{s}$ denote the irrotational field and the non-divergence field, respectively. Similarly, the force term can also be decomposed as

$$\mathbf{F} = \nabla F_\varphi + \nabla\times\mathbf{F}_\psi, \tag{18}$$

where F_φ and $\mathbf{F}_\psi$ denote the scalar potential and vector potential of $\mathbf{F}$, respectively. Substituting Eqs. (17) and (18) into Eq. (16), we obtain

$$\left[v_\mathrm{p}^2\nabla^2\mathbf{u}_\mathrm{p} + \nabla F_\varphi - \frac{\partial^2\mathbf{u}_\mathrm{p}}{\partial t^2}\right] + \left[v_\mathrm{s}^2\nabla^2\mathbf{u}_\mathrm{s} + \nabla\times\mathbf{F}_\psi - \frac{\partial^2\mathbf{u}_\mathrm{s}}{\partial t^2}\right] = 0, \tag{19}$$

where v_p denotes P-wave velocity and v_s denotes S-wave velocity.

Taking divergence and rotation to Eq.(19), respectively, we obtain

$$\nabla^2\mathbf{u}_\mathrm{p} - \frac{1}{v_\mathrm{p}^2}\frac{\partial^2\mathbf{u}_\mathrm{p}}{\partial t^2} = -\frac{\nabla F_\varphi}{v_\mathrm{p}^2}, \tag{20}$$

$$\nabla^2\mathbf{u}_\mathrm{s} - \frac{1}{v_\mathrm{s}^2}\frac{\partial^2\mathbf{u}_\mathrm{s}}{\partial t^2} = -\frac{\nabla\times\mathbf{F}_\psi}{v_\mathrm{s}^2}. \tag{21}$$

From Eqs. (20) and (21), we know that the P- and S-wave equation has a similar form. Analogous to the calculation of the P-wave envelope field in the acoustic case, the S-wave equation can also approximately simulate the propagation of the energy. Therefore, the S-wave envelope field can be approximately calculated by taking the envelope of the S-wave field.

We conduct a test to calculate the elastic envelope field in the strong-scattering cases. The parameters are the same as the test in Fig. 2. We calculate the envelope field of P- and S-waves and extract the snapshots at 0.6 s, which are shown in Fig. 3a and b, respectively. Compared with Fig. 2d and e, we know that the P- and S-wave envelope fields contain more abundant low-frequency information and reflect the macroscopic fluctuation of the wavefields, which have great potential for the inversion of large-scale structures of the subsurface media.

3.3. Gradient calculation

As discussed above, there will be strong parameter coupling effects in the multi-parameters reconstruction of the strong-scattering media. Therefore, we calculate the gradient of EDEI with the help of the wave mode decomposition method to enhance the parameter decoupling. The main idea is to separate the P- and S-wave envelope field, and then use the envelope field of different mode to update the v_p and v_s according to their contributions to the parameter perturbation.

From the radiation pattern analysis (Wang and Cheng, 2017), we know that the P-wave velocity perturbation only generates P-wave

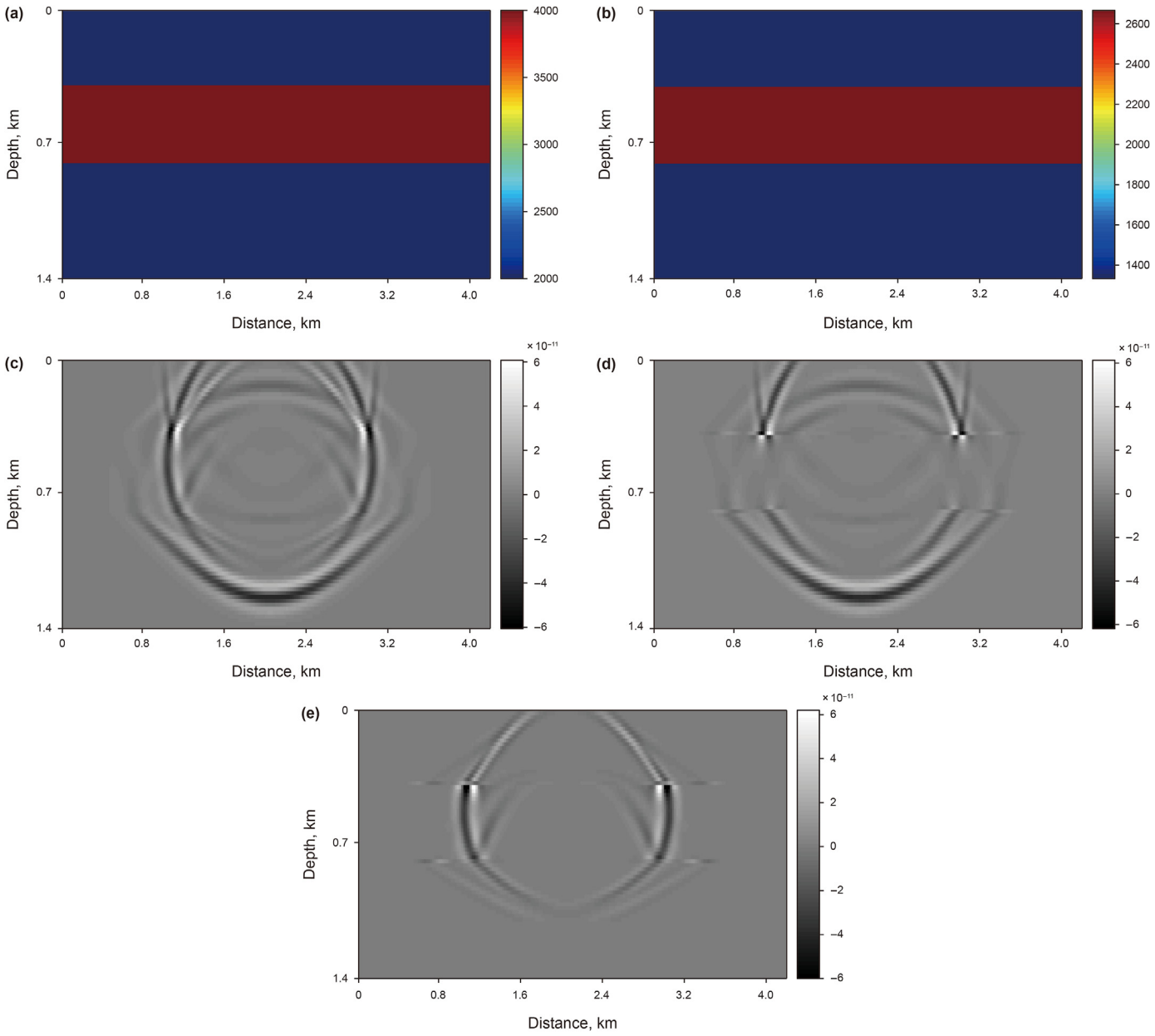

Fig. 2. Test of elastic wave mode decomposition. (a) and (b) are the true Vp and Vs model, respectively; (c) is the z-component snapshot at 0.6 s; (d) and (e) are the decomposed z-component P and S wavefield, respectively.

scattering. In other words, the contributions to the P-wave velocity update only come from the P-waves. Therefore, the P-wave velocity can be updated using

$$\frac{\partial J_3}{\partial \mathbf{v}_\mathrm{p}} = -2\rho \mathbf{v}_\mathrm{p} \sum_{sr} \int_0^T E_{\mathrm{syn}}^{\mathrm{p}} \left[G_\mathrm{e}^{\mathrm{T}}(\Delta E) \right]_\mathrm{p} \mathrm{d}t, \tag{22}$$

where $E_{\mathrm{syn}}^{\mathrm{p}}$ denotes the forward-propagating P-wave envelope field, ΔE denotes envelope data residual, $[\cdot]_\mathrm{p}$ denotes decomposed P-wave component, G_e^T denotes the transpose operator of the Green's function (envelope back-propagating operator). Here we use wavefield back-propagating operator to approximately simulate the propagation of energy (amplitude information), because for smooth background media without sharp interfaces, the wave equation can propagate relatively accurate amplitude information about the envelope field (Zhang et al., 2018).

After obtaining the v_p gradient, there are two approaches to calculate the v_s update. One approach is to calculate the v_s or v_s gradient according to the petrophysical relation between v_p and v_s. The other approach is to calculate the v_s gradient independently with the help of the wave mode decomposition method. From the radiation pattern analysis (Wang and Cheng, 2017), the perturbation of S-wave velocity can generate both P-wave scattering and S-wave scattering. However, we can see that the scattered S-waves are only due to the S-wave velocity perturbation. And if we use a P-wave source, the recorded S-waves are all converted S-waves and only has relation with S-wave velocity perturbation. Based on the gradient formula of EFWI and the wavefield radiation pattern

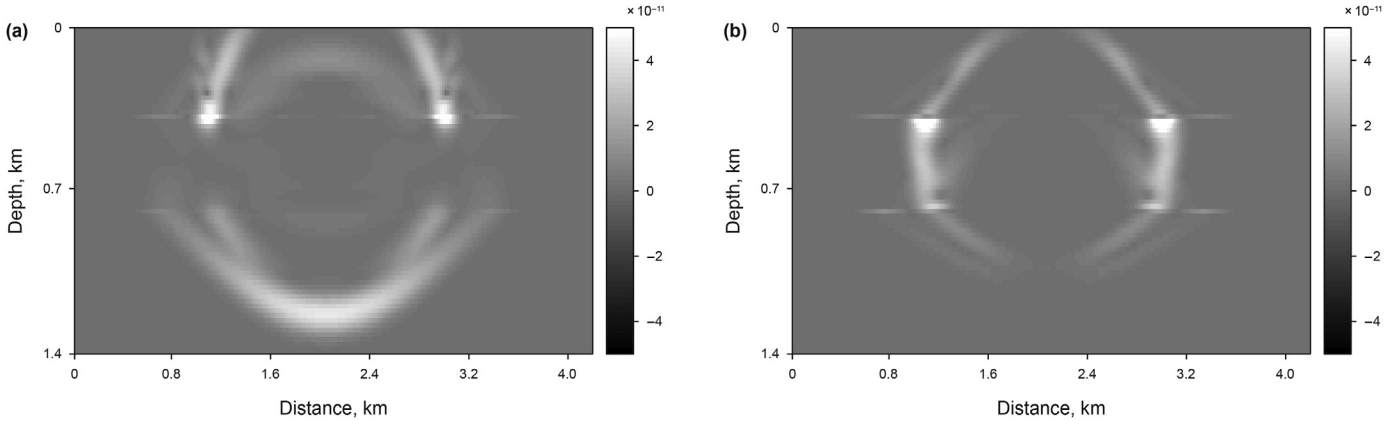

Fig. 3. Example of elastic envelope field calculation. (a) and (b) are the P-wave envelope field and S-wave envelope field, respectively.

analysis, the S-wave velocity can be updated approximately using

$$\frac{\partial J_3}{\partial \mathbf{v}_s} \approx -2\rho \mathbf{v}_s \sum_{sr} \int_0^T \left(E_{syn}^{s,x} \left[G_e^T(\Delta E) \right]_{s,x} + E_{syn}^{s,z} \left[G_e^T(\Delta E) \right]_{s,z} \right) \Big/ \mu^2 \mathrm{d}t, \tag{23}$$

where $E_{syn}^{s,x}$ and $E_{syn}^{s,z}$ denote x and z components of the forward-propagating S-wave envelope field, respectively; $[\cdot]_{s,x}$ and $[\cdot]_{s,z}$ denote x and z components of the decomposed S-wave components, respectively. Eq. (23) ignores the complex conversion effects of P and S waves and only considers the contribution of SS mode, which is just an approximate equation. In general, the vector fields contain direction (angle) information, so it will change the imaging amplitude. However, in the current studies, the vector dot product method has little effect on Vs update. The current envelope calculation ignores the polarity information and only considers the instantaneously amplitude information. The very low-wavenumber update provided by vector fields product reflects relatively good salt dome information.

In the following, we test the gradients of EDEI using the above-proposed methods. The true Vp and Vs models are shown in Fig. 4a and b, respectively. There is a high-velocity layer in the true model. The vertical range of the layer in Vp is 220–600 m and in Vs is 420–800 m. This may not have a clear or real geological significance but is very feasible for testing the decoupling effects of the proposed method. The initial Vp and Vs models are homogeneous models, which are shown in Fig. 4c and d, respectively. The source wavelet is a low-cut Ricker wavelet with a dominant frequency of 9 Hz. The information below 4 Hz is cut off. There are 52 sources uniformly set on the surface with a source interval of 80 m. The recording time is 2.5 s and the sampling interval is 2 ms. The Vp and Vs gradients are shown in Fig. 4e and f. Since the update direction is the negative direction of the gradient, the blue color means enhancing the velocity of the initial model. We can see that both Vp and Vs gradients provide relatively good update directions in the position of high-velocity layer. The update of Vs inside the target layer is not uniform, which means the update of Vs is more difficult than that of Vp. However, the update direction in Vs gradient can still show the characteristics of the strong-scattering layer.

3.4. Inversion strategies

The primary inversion strategy used in this paper is the multi-scale inversion strategy. The EDEI is used to reconstruct the large-scale structures of the strong-scattering media, and then the EFWI is used to invert more fine structures of the media. The results of EDEI is set as the initial models of the EFWI. In EFWI, we also use the multiscale inversion strategy. The observed data is decomposed into different frequency bands, and we invert from the low-frequency band to the high-frequency band successively. The results obtained in the current scale is set as the initial models of the next scale. The EFWI used in this paper is the conventional one and wave mode decomposition strategy is not used. Like EFWI, the EDEI also can be a multiscale inversion. Especially for very large-scale salt inversion, the multiscale EDEI is very important to invert the salt body information from the background velocity model. However, the salt scale used in this paper is moderate. Therefore, we only conduct EDEI in one scale. For the choose of frequency band, we can filter the envelope and conduct gradient test. Then we can judge whether this frequency band is suitable according to the salt perturbation shown in the gradient result. The optimization approach we used for EDEI is the steepest descent method, and for EFWI is the conjugate gradient method.

4. Numerical examples

4.1. EDEI with a preliminary Vp to Vs ratio

In this test, we mainly construct Vp and Vs by EDEI based on petrophysical relation. In some cases, we may know an initial estimate of Vp to Vs ratio or the Poisson's ratio of the study areas. If the Vp to Vs ratio is accurate, the inversion process will converge easily. However, in most cases the Vp to Vs ratio is only an initial estimate. Therefore, in our test, we first invert Vp using EDEI method, and calculate Vs according to the preliminary Vp to Vs ratio, then conduct EFWI using the inverted Vp and estimated Vs as initial models.

We test the proposed method in a layered salt model. The P-wave velocity of the salt layer is 4000 m/s with a thickness of about 400 m. The background P-wave velocity is 2000 m/s. The true and initial velocity models are shown in Fig. 5 and Fig. 6, respectively. The depth shallower than 200 m is assumed to be water layer and the velocity is known. There is no prior information on the salt layer in the initial models. The source wavelet is a low-cut Ricker wavelet with a dominant frequency of 9 Hz. The information below 4 Hz is cut off. Considering the source wavelet bandwidth and the velocity contrast, this is a typical large-scale and strong-scattering inversion case. Firstly, we conduct conventional EFWI, and the result after 300 iterations is shown in Fig. 7. We can see that the conventional EFWI method can only obtain the top boundary information of the salt layer. The inverted Vs salt layer is thicker than the inverted Vp

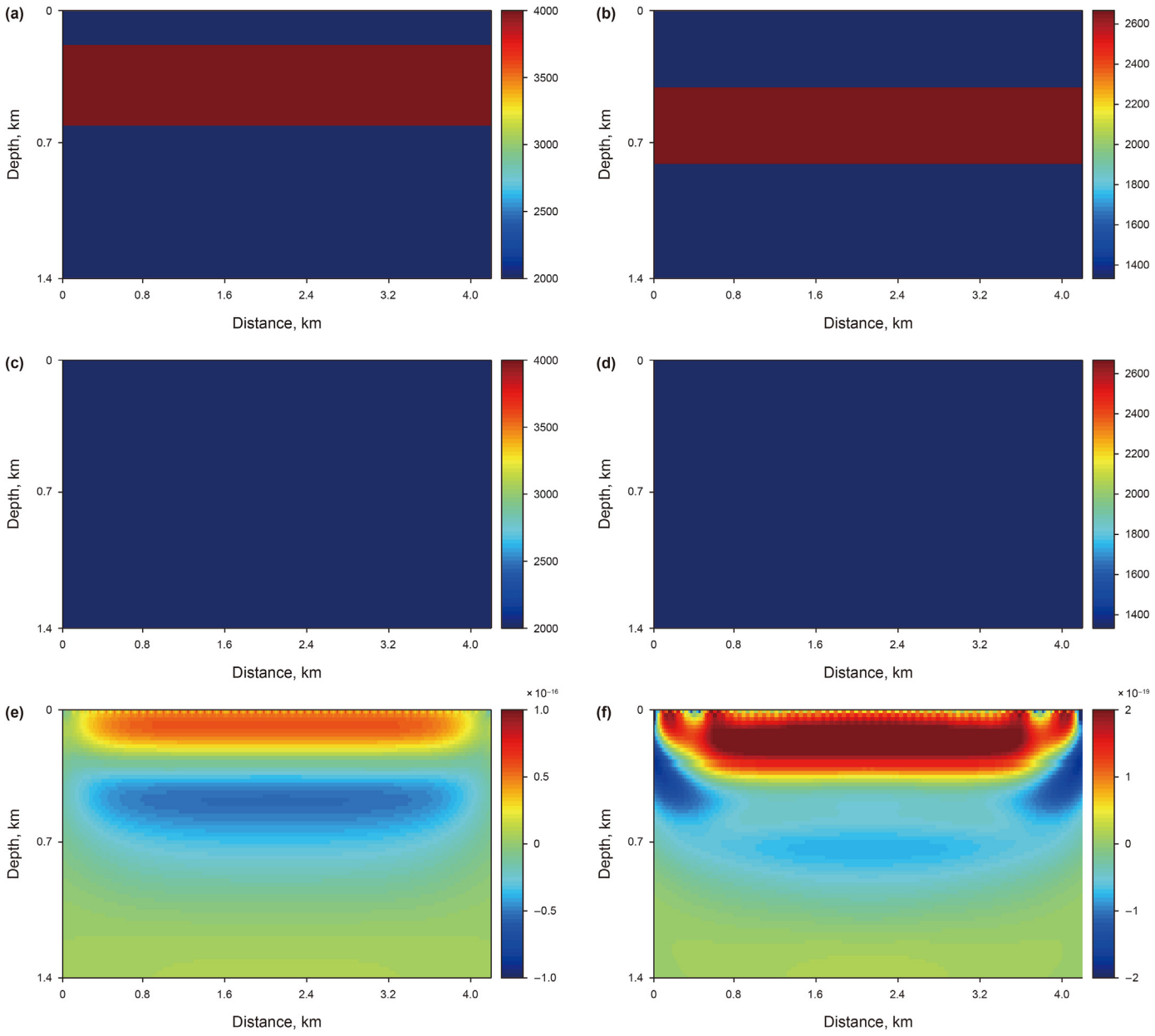

Fig. 4. Gradient test of EDEI method. (a) and (b) are the true Vp and Vs models, respectively; (c) and (d) are the initial Vp and Vs models, respectively; (e) and (f) are the gradients of Vp and Vs, respectively.

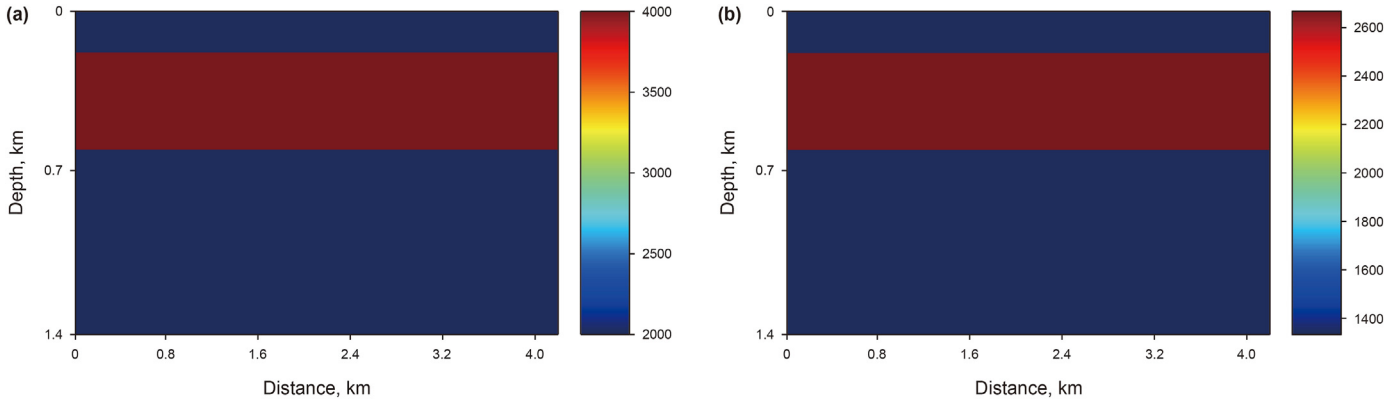

Fig. 5. The true velocity models. (a) and (b) are the true Vp and Vs models, respectively.

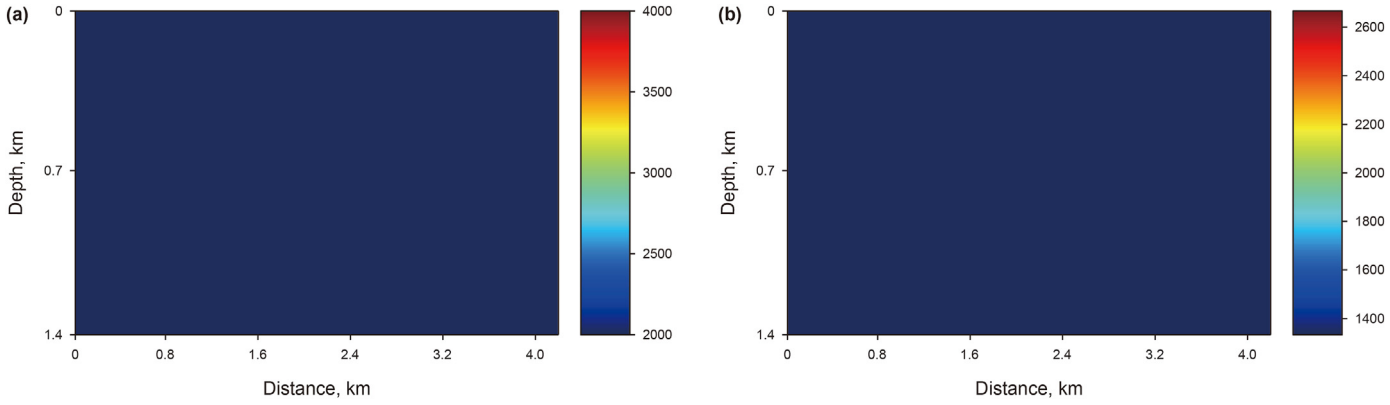

Fig. 6. The initial velocity models. (a) and (b) are the initial Vp and Vs models, respectively.

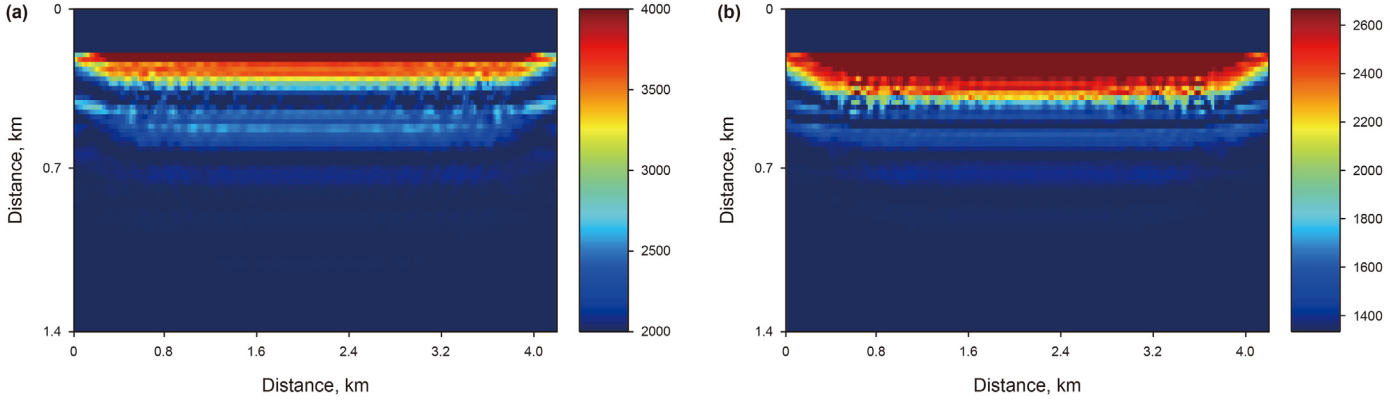

Fig. 7. The inversion results of conventional EFWI. (a) and (b) are the inverted Vp and Vs models, respectively.

salt layer because the velocity contrast of Vs model is weaker than that of the Vp model. Then we use the proposed EDEI method to recover the Vp and Vs of the salt model. The true Vp to Vs ratio is 1.5. Here we assume that we have got a preliminary Vp to Vs ratio, which is 2. The inverted Vp model after 50 iterations is shown in Fig. 8a. We calculated Vs (Fig. 8b) using Fig. 8a according to the preliminary Vp to Vs ratio. Using Fig. 8a and b as initial model, the conventional EFWI results after 250 iterations are shown in Fig. 8c and d. We can see that although the final inversion results are better than the conventional EFWI method (Fig. 7), the strong-scattering salt layer is still not inverted well because of the inaccurate Vp to Vs ratio. The single trace comparison of the inversion results is shown in Fig. 9. We can see that the EDEI provides the long-wavelength information of the salt layer. The value of Vs calculated using wrong Vp to Vs ratio (green line in Fig. 9b) has obvious errors. The final Vs result (blue line in Fig. 9b) can reflect the characteristics of about half of the salt layer thickness, but the final Vp result (blue line in Fig. 9a) can only provide the accurate top boundary information of the salt layer.

4.2. EDEI with an independent update of Vs

In some cases, if we obtain relatively accurate Vp to Vs ratio or the Poisson's ratio of the study areas, the reconstruction of the multi-parameter strong scatters will be relatively easy because accurate petrophysical constraint helps to reduce the nonlinearity of the inversion process. However, if the Vp to Vs ratio is just a rough estimation, the convergence of the EDEI process may be incomplete just like the test in section 4.1. The independent Vs update method based on wave mode decomposition can make up for the disadvantages of the inaccurate petrophysical constraint, but the decoupling of multi-parameters for different Vp and Vs structures still remains a problem for the current EDEI algorithm. Therefore, in real applications, we suggest to use reliable petrophysical information as constraint for the EDEI process if available, and then update Vs independently in EDEI to obtain the final inversion result.

In this test, based on the inversion result shown in Fig. 8a and b, we update Vs independently during the EDEI process using Eq. (23). Firstly, the Vp is kept as Fig. 8a (now shown in Fig. 10a), we only update Vs using Fig. 8b as the initial model. The inverted Vs by EDEI after 15 iterations is shown in Fig. 10b. We can see that the Vs value of the salt layer is increased and closer to the true Vs model compared with Fig. 8b. Using Fig. 10a and b as the initial model, the conventional EFWI results after 250 iterations are shown in Fig. 10c and d. We can see that the internal velocity of the salt layer is more uniform than Fig. 8c and d. The bottom boundary of both Vp and Vs salt layer is reconstructed clear. The single trace comparison of the inversion results is shown in Fig. 11. Comparing Figs. 11a and 9a, we know that the final inversion result can provide better Vp information of the salt layer, not only for the internal velocity but also for the bottom boundary. Comparing Figs. 11b and 9b, we know that the Vs value is enhanced and closer to the true value after independent update by EDEI. The final Vs result can better reflect the characteristics of the salt layer. After comparison, we know that updating Vs independently after the inversion using preliminary Vp to Vs ratio in EDEI can lead to better final inversion results.

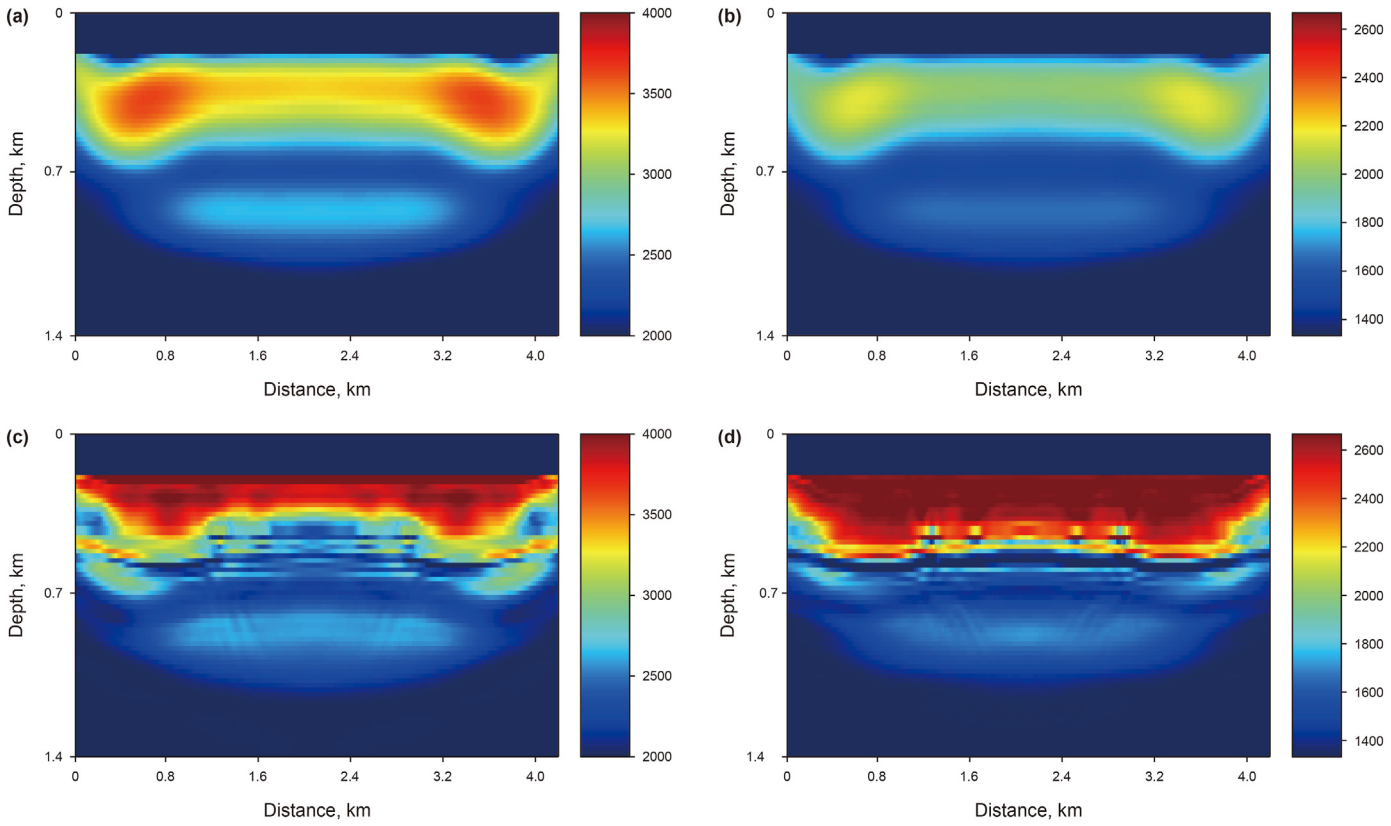

Fig. 8. The inversion results of EDEI with an initial estimate of the Vp to Vs ratio. (a) is the inverted Vp model by EDEI; (b) is the Vs model calculated using (a) according to the initial estimate of Vp to Vs ratio; (c) and (d) are the inverted Vp and Vs models by EDEI + EFWI.

4.3. Noise-free data test on the SEG/EAGE salt model

Now we test the proposed method on the SEG/EAGE salt model. For the estimation of Vs, we have proposed two strategies in this paper. In some complex cases or real cases, the prior petrophysical information may help a lot and should be used. In some cases, we may know nothing about the Vp to Vs ratio of unknown models. In these cases, we can choose the second strategy and update Vs directly using wave mode decomposition, which is shown in the following test. The true velocity models are shown in Fig. 12. There is a salt dome in the middle of the model. The P-wave velocity of the salt dome is 4482 m/s and the background P-wave velocity is about 2000 m/s. The S-wave velocity of the salt dome is about 3000 m/s and the background S-wave velocity is about 1300 m/s. The initial velocity models are shown in Fig. 13. There is no prior information on the salt body in the initial model. The source wavelet is a low-cut Ricker wavelet with a dominant frequency of 9 Hz. The information below 3 Hz is cut off. The sources and receivers are uniformly located on surface with source interval 160 m and receiver interval 20 m. Firstly, we conduct the conventional EFWI and the results after 430 iterations are shown in Fig. 14. We know that conventional EFWI can only invert some top boundary information of the salt body without enough low-frequency information. The inverted top boundaries of the salt body in Vs model is better than that in Vp model. Using the same initial models, the conventional elastic envelope inversion (EEI) results after 130 iterations are shown in Fig. 15. We can see that the EEI can provide more low-wavenumber information than the EFWI method, but still cannot recover any useful information about the large-scale salt body. Then we conduct inversion using the proposed EDEI method and the results after 35 iterations are shown in Fig. 16a and b. We can see that both the large-scale Vp and Vs structures are recovered well. Using Fig. 16a and b as the initial models, the multiscale EFWI results are shown in Fig. 16c and d. The frequency-bands used in the multiscale EFWI is 3–7 Hz and then 3–20 Hz, and the iteration numbers are 150 and 270, respectively. Compared with the conventional inversion results (Fig. 14), we know that the proposed method can enhance the inversion quality of the multi-parameter strong-scattering structures. In addition to the salt body reconstruction, the shallow weak scattering structures and some subsalt structures are recovered well. The objective function curves of the inversion process are shown in Fig. 17. All the curves show fast and stable convergence. From the declining ratio of the objective function value, we know that the EEI result is better than the EFWI result and the EDEI + EFWI result provide the best result.

4.4. Noisy data test on the SEG/EAGE salt model

Now we conduct anti-noise test of the proposed method. We still use the true velocity models and the initial velocity models shown in Figs. 12 and 13. The acquisition parameters and source wavelet are the same as the above test. The noisy records of z- and x-components are shown in Fig. 18a and b, respectively. We can see that some weak reflection events are covered by random noise. Using the noisy data as observed data, we conduct EDEI and the results after 35 iterations are shown in Fig. 19a and b. We can see that the strong-scattering salt information is still clearly recovered. Compared with Fig. 16a and b, we know that the Vp result is almost unaffected by noise, but the reflection of the salt dome in the Vs result is slightly weaker. Using Fig. 19a and b as initial models, the multiscale EFWI results are shown in Fig. 19c and d. The frequency bands of the multiscale EFWI are 3–7 Hz and 3–20 Hz, and the

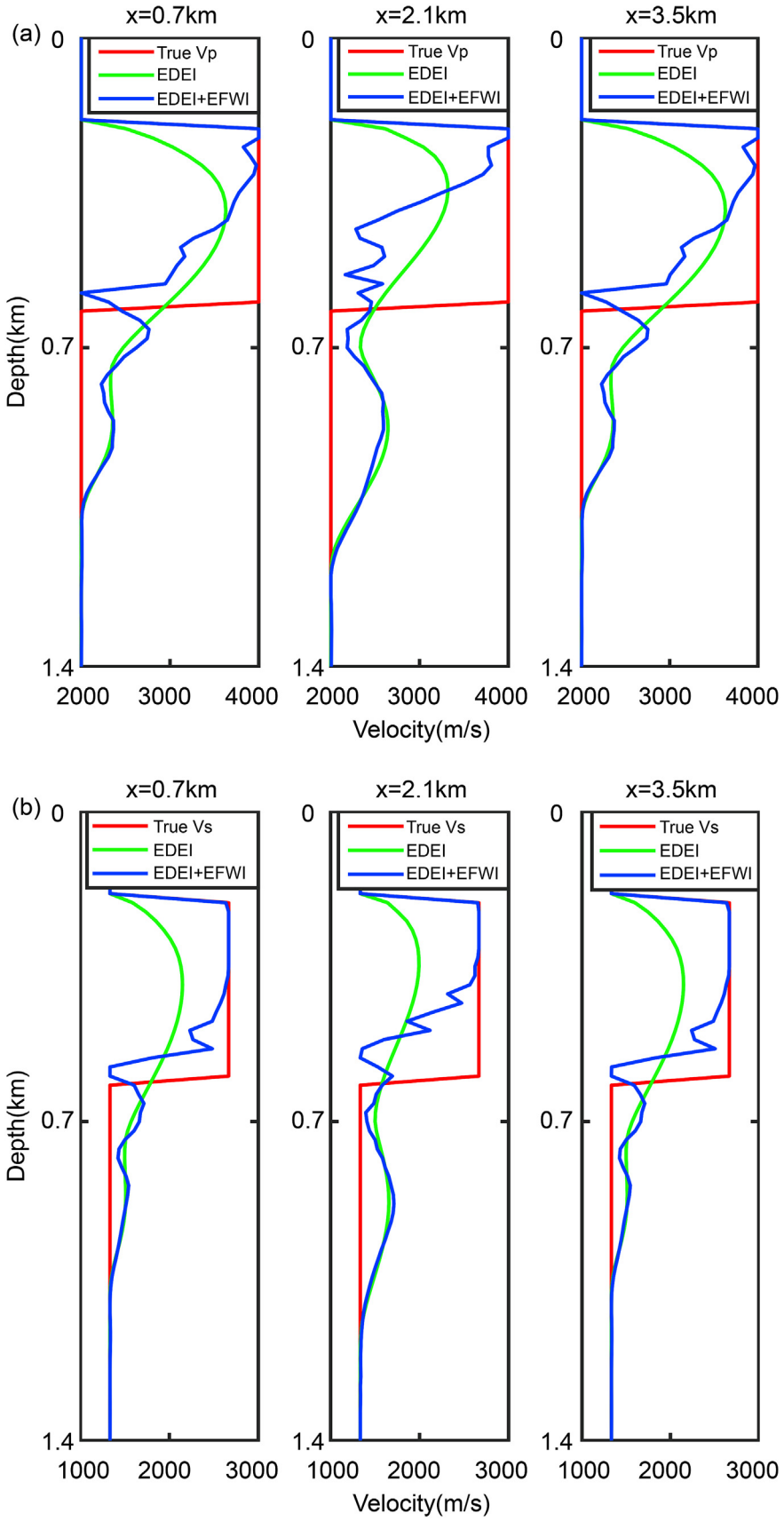

Fig. 9. Single trace comparison of Fig. 8. (a) is the single trace comparison of Vp; (b) is the single trace comparison of Vs.

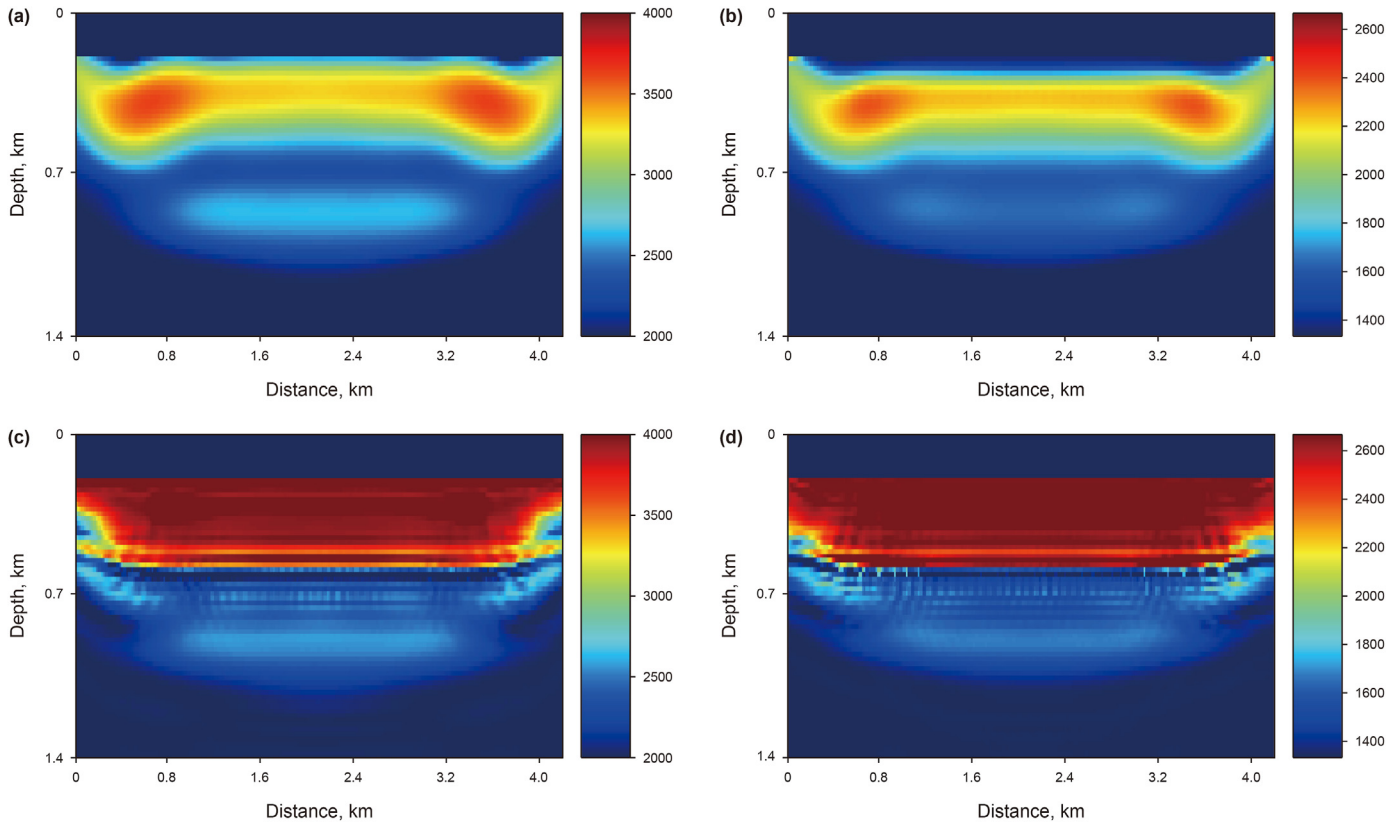

Fig. 10. The inversion results of EDEI with independent Vs update. (a) is the same as Fig. 8a; (b) is the Vs model inverted independently by EDEI; (c) and (d) are the inverted Vp and Vs models by EDEI + EFWI.

iteration numbers are 150 and 270, respectively. The boundaries of the salt body are well recovered and the shallow weak scattering structures are recovered well. Although affected by noise, there are still some subsalt structures inverted due to a good salt body reconstruction. Overall, the proposed method can achieve good results at this moderate noise level.

5. Discussion

5.1. Elastic envelope field calculation and the polarity information

The envelope field calculation in elastic media is similar to that in acoustic media (Zhang et al., 2018). We first calculate the elastic wavefield using the Ricker wavelet as source. Then we conduct wave mode decomposition according to this paper to obtain the P and S wavefield. Taking envelope of these 3D wavefields, we can obtain the forward-propagated P and S envelope wavefield. In the proposed EDEI method, the wave mode decomposition algorithm is based on Helmholtz's equation. This traditional wave mode decomposition algorithm ignores the conversion between P- and S-waves at the current separation time (Tang and McMechan, 2018). This will cause separation errors at strong-contrast interfaces (see Figs. 2 and 3). From our researches, the separation artifact will affect the interface information of the EDEI result. However, the current EDEI method can still provide good large-scale update of strong-contrast salt bodies.

For backward-propagated envelope wavefield, the adjoint source is the envelope data residual. In this paper, the forward-propagated envelope wavefield has no polarity because the envelope is calculated with the help of Hilbert transform. However, the backward-propagated envelope wavefield has polarity information because the adjoint source has polarity information. For the strong low velocity perturbation cases, the proposed method still works. In the salt models, the top boundary of salt bodies are strong high velocity perturbations and the bottom boundary of salt bodies are strong low velocity perturbations. The DEI and EDEI methods can handle both these two strong scattering cases. In addition, some researchers have proposed some other envelope calculation approaches to retain polarity information in the envelope wavefield, which achieve good results (Chen, 2018b). The inversion results will be better if these polarized envelope calculation approaches are introduced into the EDEI method.

5.2. Calculation efficiency

The calculation cost of EDEI is mainly spent on the forward modeling. The P and S envelope fields are calculated after separating the P and S wavefields. Actually, we do not need to store the whole wavefield in the mode decomposition process, because the partial derivatives in Eqs. (14) and (15) are solved by the finite difference of elastic wave equation. Therefore, by modifying the forward modeling algorithm, the P and S wavefields can be directly calculated. However, for the P and S envelope fields calculation, we should store the whole P and S wavefields. The calculation efficiency of the proposed EDEI method in each iteration is similar with the EFWI based on wave mode decomposition but lower than the conventional EFWI method.

5.3. Potential improvements for multi-parameter inversion

From Eq. (23) we know that the current Vs gradient derivation has a SS wave approximation. The PS wave mode is always strong

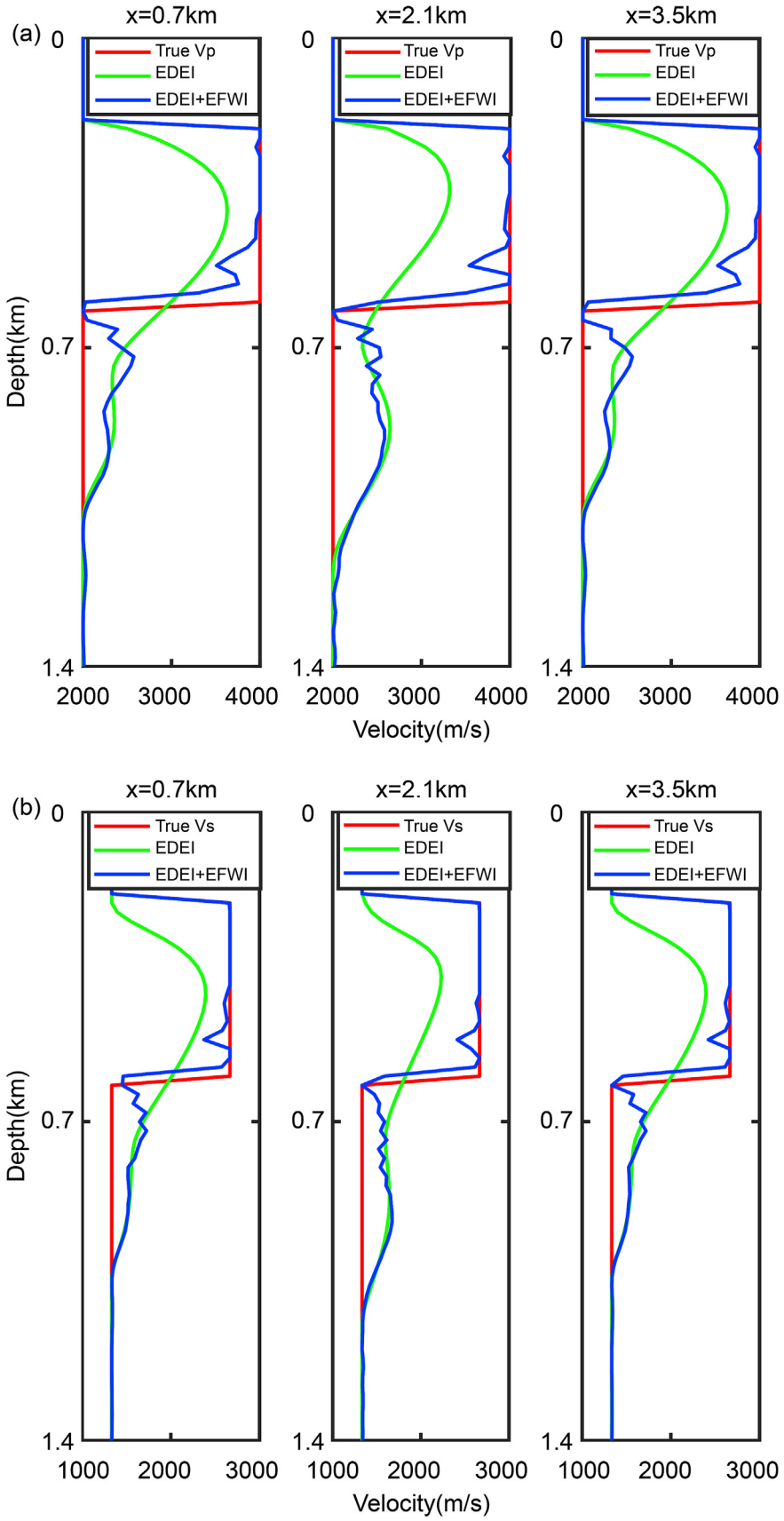

Fig. 11. Single trace comparison of Fig. 10. (a) is the single trace comparison of Vp; (b) is the single trace comparison of Vs.

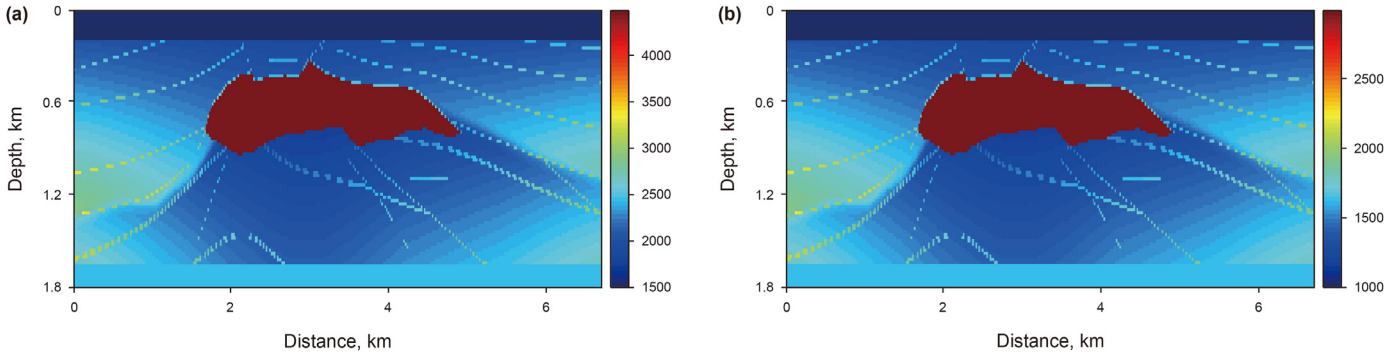

Fig. 12. The true velocity models. (a) and (b) are the true Vp and Vs models, respectively.

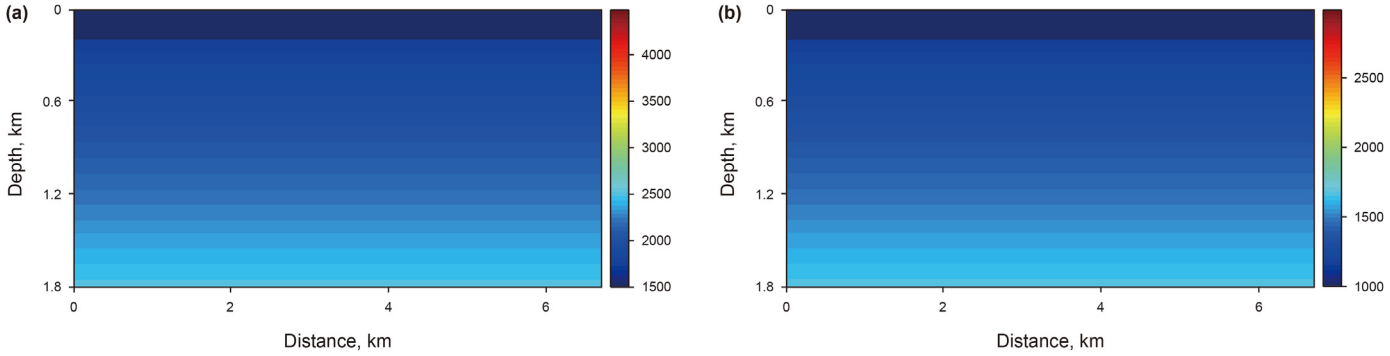

Fig. 13. The initial velocity models. (a) and (b) are the initial Vp and Vs models, respectively.

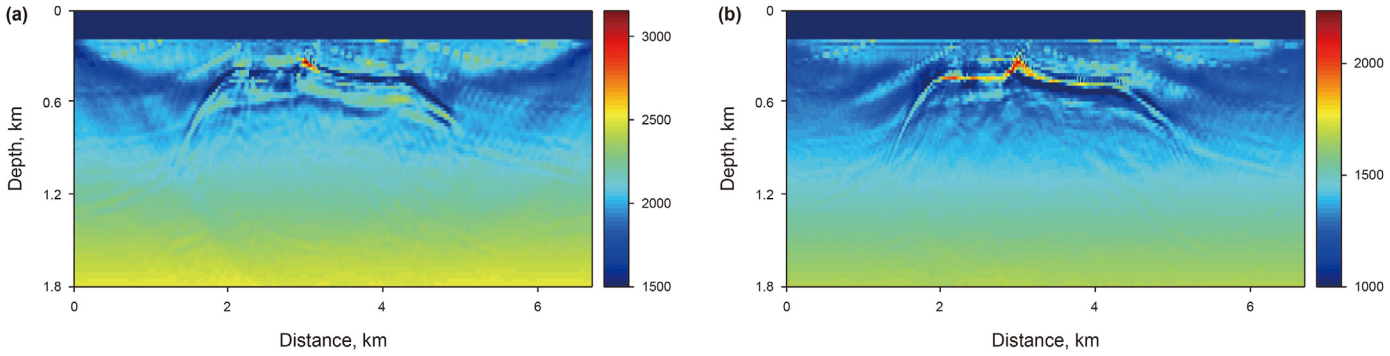

Fig. 14. The inversion results of conventional EFWI. (a) and (b) are the inverted Vp and Vs models, respectively.

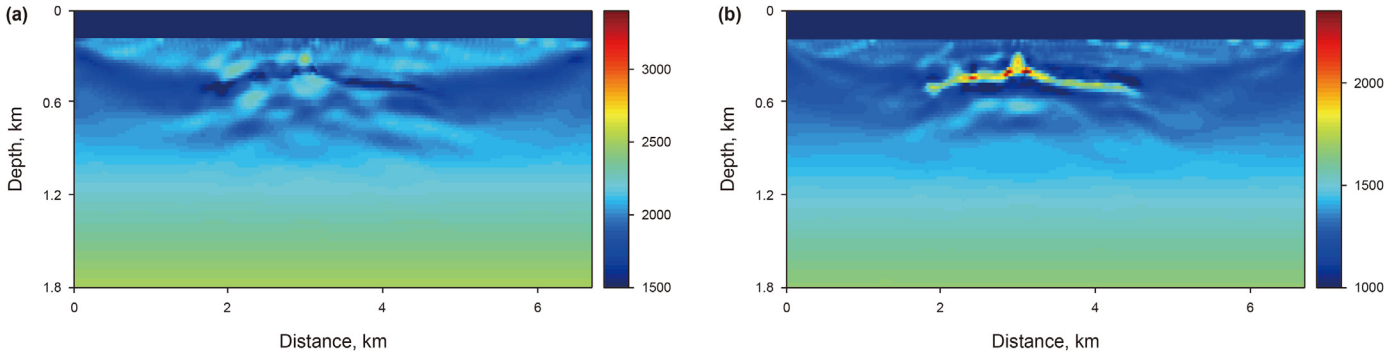

Fig. 15. The inversion results of conventional EI. (a) and (b) are the inverted Vp and Vs models, respectively.

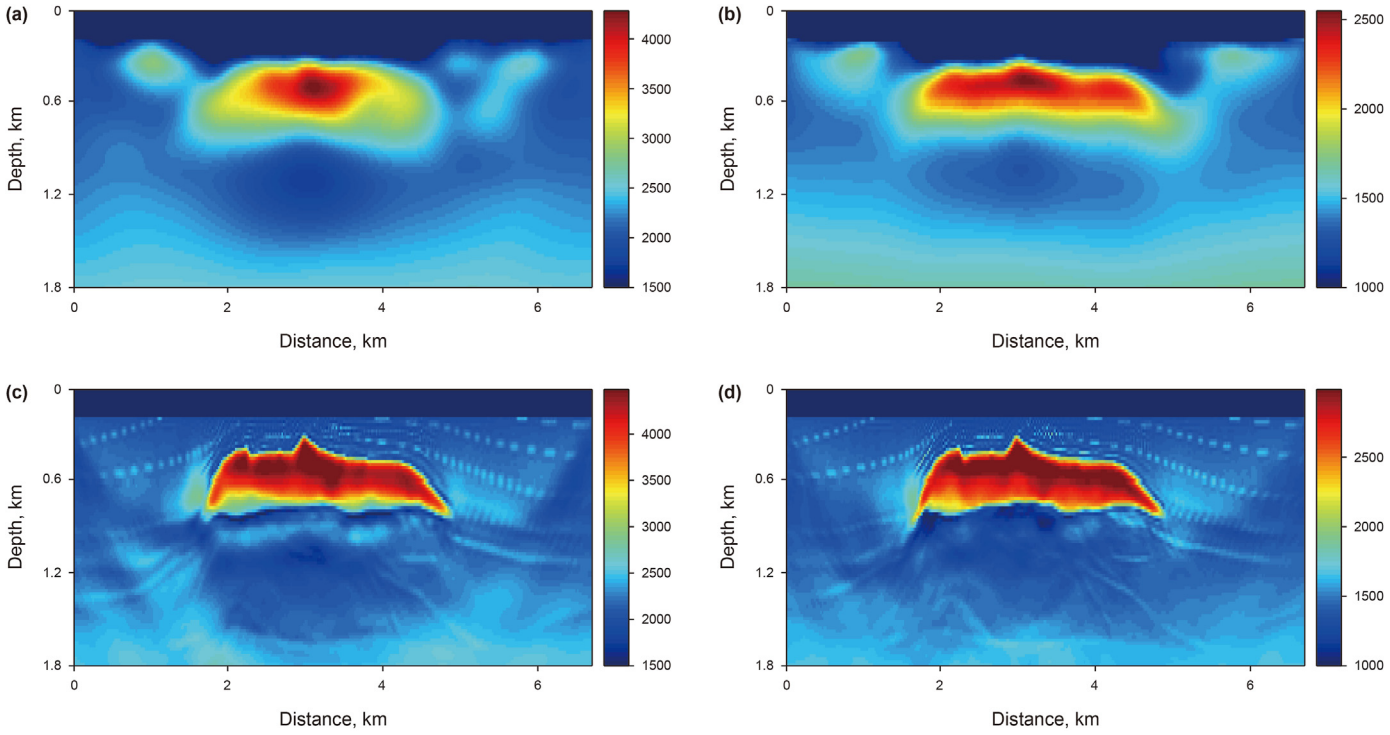

Fig. 16. The inversion results of EDEI. (a) and (b) are the inverted Vp and Vs models by EDEI, respectively; (c) and (d) are the multiscale EFWI results using (a) and (b) as initial models.

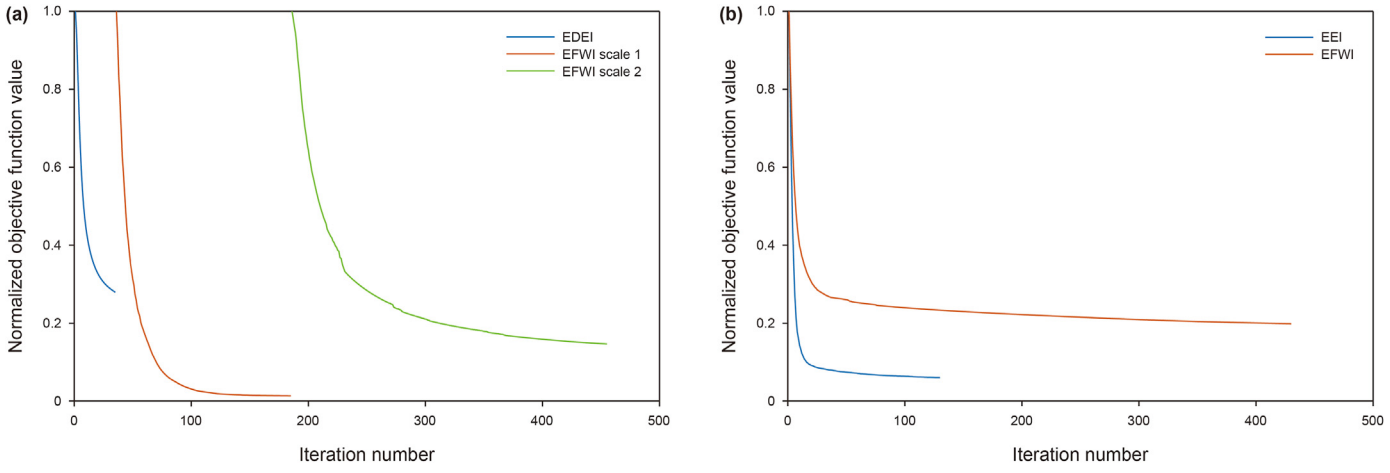

Fig. 17. Objective function curves of the inversion process. (a) shows the objective function curves of the EDEI + EFWI process. (b) shows the objective function curves of the EEI and EFWI process.

and should be used for multi-parameter inversion. However, before using PS waves to update the velocity change in EDEI, we should study further to the linearity of P–S conversion to Vs dependence, which is currently in preliminary research. After finishing the related research, the P–S converted wave can be better used to update the Vs model. The current SS approximate gradient equation can solve the strong-scattering Vs update to some extent, which can be seen in the numerical tests. However, it also causes some problems, such as the difficulty in the inversion of different Vp and Vs structures, especially in strong velocity contrast cases, which can be seen in Fig. 4. I think it is a good research direction in the future to make full use of the PS converted waves in EDEI method.

In the current research, we only invert Vp and Vs by the proposed EDEI method. The inversion of density parameter is different from that of λ and μ, because the seismic data perturbation is not very sensitive to large scale density perturbation. Therefore, the inversion of large-scale density structures is more difficult than the inversion of large-scale velocity structures for FWI and DEI methods. For acoustic DEI, there are some preliminary researches for density inversion (Luo et al., 2020). The inversion of density is actually based on angle domain wavefield decomposition and petrophysical relation. In elastic case, Eq. (11) is appropriate for density, but to obtain better density inversion results, more inversion strategies, such as wavefield direction decomposition, need to be studied.

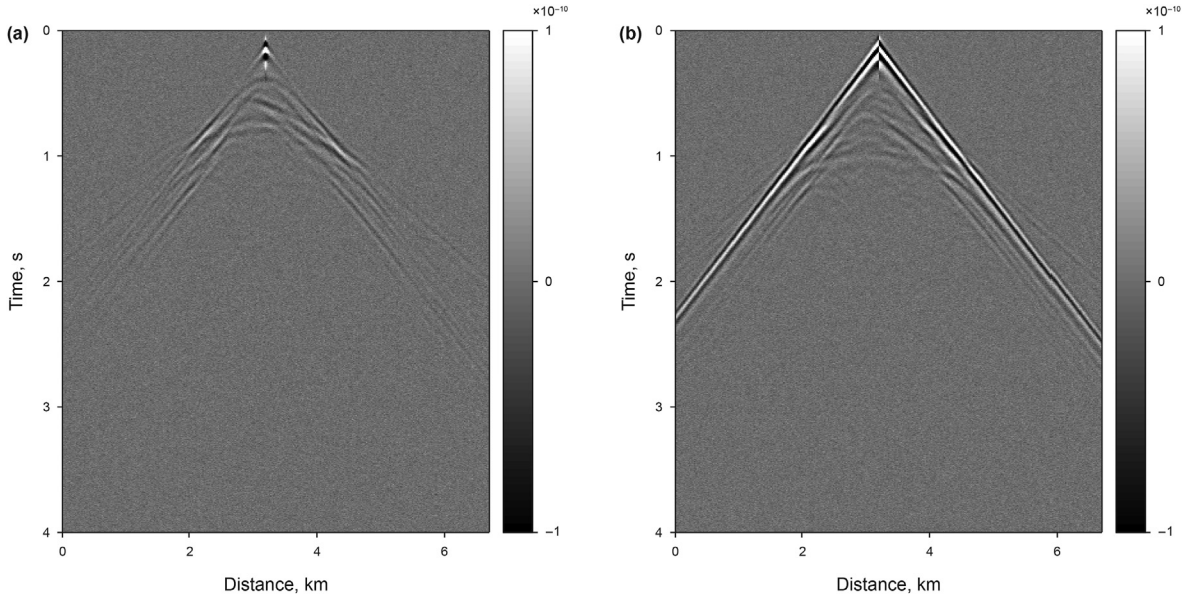

Fig. 18. Noisy data used for inversion. (a) and (b) are the z- and x-components, respectively.

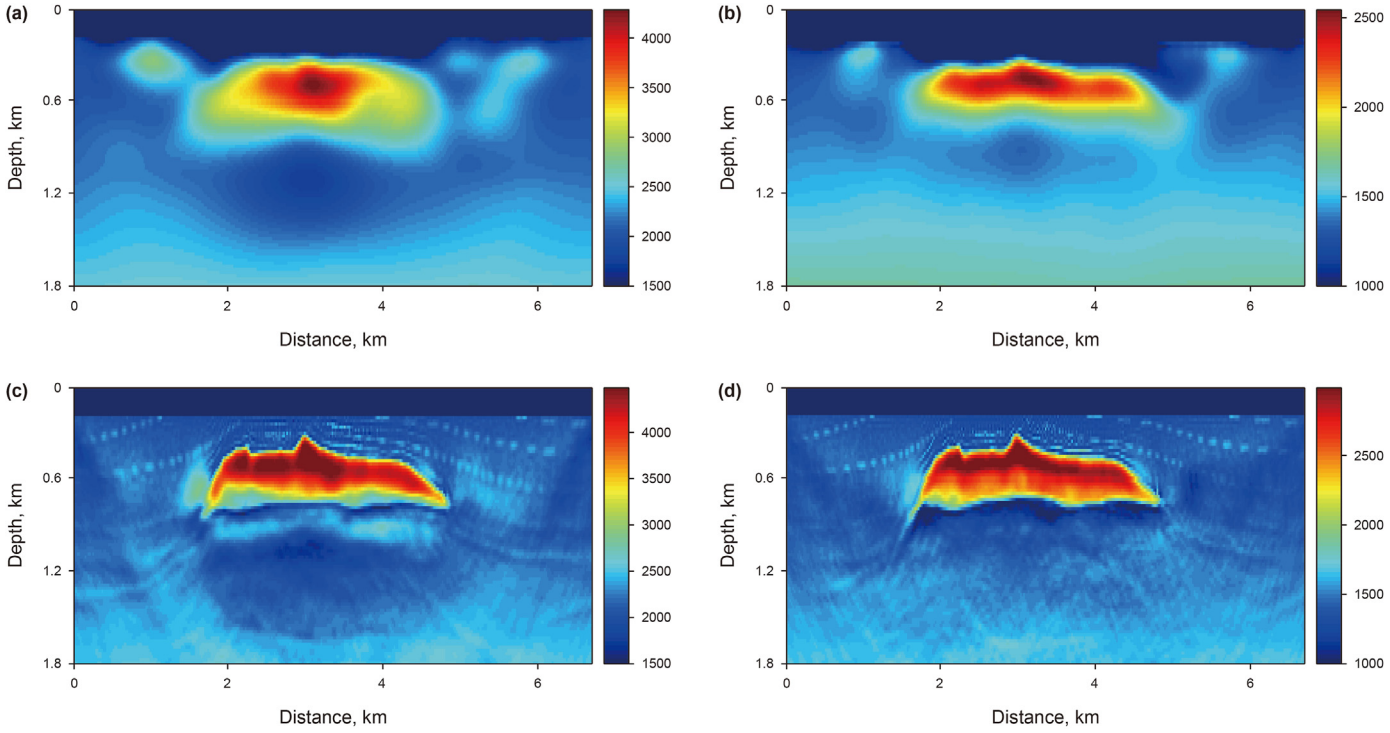

Fig. 19. The inversion results of EDEI using noisy data. (a) and (b) are the inverted Vp and Vs models by EDEI, respectively; (c) and (d) are the multiscale EFWI results using (a) and (b) as initial models.

In addition, in the process of EDEI, we do not separate the P and S wave recordings, because it is always very difficult in real cases. Therefore, in the proposed EDEI method, the propagation operator is separated but the seismic records or adjoint source are not separated to P and S waves. If we use separated P and S waves, the decoupling process may be easier and the final result may further improve.

5.4. Issues on real data application

For real data application of the proposed EDEI method, there are at least three problems need to be solved to improve the robustness of the inversion process. One problem is the inaccurate source wavelet. Like DEI method (Zhang et al., 2018), the EDEI method is also sensitive to source wavelet errors. Source wavelet is the initial condition of the forward modelling algorithm. Any amplitude and

phase error will influence the synthetic seismic waveform and may have obvious effects on the final inversion results. To mitigate the effects of source wavelet errors, the source-independent algorithm is a good choice (Zhang et al., 2018). One problem is complex real noises contained in seismic records. Real noise is different from synthetic noise, like Gaussian noise. They may have strong energy, unbalanced distribution and time or spatial coherence. Therefore, denoising is a very important process before conducting inversion. Another problem is amplitude errors or imbalance. There are many factors may influence the amplitude of seismic records, including attenuation, density variation, elastic effects, data processing parameters, and so on. Therefore, to accurately match the amplitude information is very difficult. The global or local cross-correlation algorithm may help to reduce the influences of amplitude errors in the inversion process.

6. Conclusions

We propose an EDEI method based on wave mode decomposition which can reconstruct the multi-parameter strong-scattering structures without the need of low-frequency data and any prior information. The proposed EDEI method can reconstruct reliable large-scale Vp and Vs models of the strong-scattering salt structures. The successive EFWI can obtain relatively high-precision inversion results of the salt model. We derive the Vp and Vs gradient using the wave mode decomposition method, which can effectively reduce the coupling effects between multi-parameters. P-waves make main contributions to the large-scale Vp update in the proposed EDEI method. We give two approaches to calculate Vs update. One is according to the petrophysical relation between Vp and Vs (Vp to Vs ratio), and the other is using the wave mode decomposition algorithm. S-waves make main contributions to the Vs update in the proposed EDEI method. The independent Vs update in EDEI can lead to better final inversion results. The tests on a layered salt model and the SEG/EAGE salt model both demonstrate the effectiveness of the proposed method. Anti-noise tests show that the proposed method can achieve relatively good results in moderate noise level.

Acknowledgments

We are thankful to three anonymous reviewers for the valuable comments and suggestions that helped to improve this manuscript. The authors greatly appreciate the financial support jointly provided by the National Key R&D Program of China under contract number 2019YFC0605503C, the Major Projects during the 14th Five-year Plan period under contract number 2021QNLM020001, the National Outstanding Youth Science Foundation under contract number 41922028, the Funds for Creative Research Groups of China under contract number 41821002 and the Major Projects of CNPC under contract number ZD2019-183-003.

References

Chen, G.X., Wu, R.S., Chen, S.C., 2018a. Reflection multi-scale envelope inversion. Geophys. Prospect. 66, 1258–1271. https://onlinelibrary.wiley.com/doi/10.1111/1365-2478.12624.

Chen, G.X., Wu, R.S., Wang, Y.Q., et al., 2018b. Multi-scale signed envelope inversion. J. Appl. Geophys. 153, 113–126. https://www.sciencedirect.com/science/article/abs/pii/S0926985117307772.

Chen, S.C., Chen, G.X., 2019. Full waveform inversion based on time-integral-damping wavefield. J. Appl. Geophys. 163, 84–95. https://www.sciencedirect.com/science/article/abs/pii/S0926985118305871.

Chen, G.X., Wu, R.S., Chen, S.C., 2019. Multiscale direct envelope inversion: algorithm and methodology for application to the salt structure inversion. Earth Space Sci. 6 (1), 174–190. https://agupubs.onlinelibrary.wiley.com/doi/10.1029/2018EA000453.

Chen, G.X., Yang, W.C., Chen, S.C., et al., 2020. Application of envelope in salt structure velocity building: from objective function construction to the full-band seismic data reconstruction. IEEE Trans. Geosci. Rem. Sens. 58 (9), 6594–6608. https://ieeexplore.ieee.org/document/9040662/.

Chi, B.X., Dong, L.G., Liu, Y.Z., 2014. Full waveform inversion method using envelope objective function without low frequency data. J. Appl. Geophys. 109, 36–46. https://www.sciencedirect.com/science/article/abs/pii/S0926985114002031.

Esser, E., Herrmann, F., Guasch, L., et al., 2015. Constraint Waveform Inversion in Salt-Affected Datasets. In: 85th SEG Annual Meeting, pp. 1086–1090. Expanded Abstract. https://library.seg.org/doi/10.1190/segam2015-5834716.1.

Esser, E., Guasch, L., Herrmann, F.J., et al., 2016. Constrained waveform inversion for automatic salt flooding. Lead. Edge 35 (3), 235–239. https://library.seg.org/doi/10.1190/tle35030235.1.

Gao, Z.Q., Li, C., Liu, N.H., et al., 2021. Large-dimensional seismic inversion using global optimization with autoencoder-based model dimensionality reduction. IEEE Trans. Geosci. Rem. Sens. 59 (2), 1718–1732. https://ieeexplore.ieee.org/document/9108603.

Guo, Z., De Hoop, M.V., 2013. Shape Optimization and Level Set Method in Full Waveform Inversion with 3D Body Reconstruction, pp. 1079–1083, 83th SEG Annual International Meeting, Expanded Abstracts. https://library.seg.org/doi/10.1190/segam2013-1057.1.

Hu, Y., Wu, R.S., Han, L.G., et al., 2019. Joint multiscale direct envelope inversion of phase and amplitude in the time-frequency domain. IEEE Trans. Geosci. Rem. Sens. 57 (7), 5108–5120. https://ieeexplore.ieee.org/document/8654734.

Lewis, W., Starr, B., Vigh, D., 2012. A Level Set Approach to Salt Geometry Inversion in Full-Waveform Inversion, pp. 1–5, 82th SEG Annual International Meeting, Expanded Abstracts. https://library.seg.org/doi/10.1190/segam2012-0737.1.

Lewis, W., Vigh, D., 2016. 3D Salt Geometry Inversion in Full-Waveform Inversion Using a Level Set Method, pp. 1221–1226, 86th SEG Annual International Meeting, Expanded Abstracts. https://library.seg.org/doi/10.1190/segam2016-13968419.1.

Liu, D.J., Huang, J.P., Wang, Z.Y., 2020. Convolution-based multi-scale envelope inversion. Petrol. Sci. 17, 352–362. https://link.springer.com/article/10.1007/s12182-019-00419-8.

Luo, J., Wu, R.S., Chen, G., 2020. Angle domain direct envelope inversion method for strong-scattering velocity and density estimation. Geosci. Rem. Sens. Lett. IEEE 17 (9), 1508–1512. https://ieeexplore.ieee.org/document/8894485.

Luo, J., Wu, R.S., Hu, Y., et al., 2022. Strong scattering elastic full waveform inversion with the envelope Fréchet derivative. Geosci. Rem. Sens. Lett. IEEE online. https://ieeexplore.ieee.org/document/9371289.

Oh, J.W., Kalita, M., Alkhalifah, T., 2018. 3D elastic full-waveform inversion using P-wave excitation amplitude: application to ocean bottom cable field data. Geophysics 83 (2), R129–R140. https://library.seg.org/doi/10.1190/geo2017-0236.1.

Peters, B., Herrmann, F.J., 2017. Constraints versus penalties for edge-preserving full-waveform inversion. Lead. Edge 36 (1), 94–100. https://library.seg.org/doi/10.1190/tle36010094.1.

Plessix, R.E., 2006. A review of the adjoint-state method for computing the gradient of a functional with geophysical applications. Geophys. J. Int. 167 (2), 495–503. https://onlinelibrary.wiley.com/doi/10.1111/j.1365-246X.2006.02978.x.

Pratt, R.G., Shin, C., Hick, G.J., 1998. Gauss-Newton and full Newton methods in frequency-space seismic waveform inversion. Geophys. J. Int. 133, 341–362. https://onlinelibrary.wiley.com/doi/10.1046/j.1365-246X.1998.00498.x.

Qu, Y.M., Li, J.L., Li, Z.C., et al., 2018. An elastic full-waveform inversion based on wave-mode separation. Explor. Geophys. 49 (4), 530–552. https://www.publish.csiro.au/EG/EG16158.

Ravaut, C., Alerini, M., Pannetier-Lescoffit, S., et al., 2008. Sub-salt Imaging by Full-Waveform Inversion: a Parameter Analysis. In: SEG Annual International Meeting, pp. 1940–1944. Expanded Abstracts. https://library.seg.org/doi/10.1190/1.3059398.

Ren, Z., Liu, Y., 2016. A hierarchical elastic full-waveform inversion scheme based on wavefield separation and the multistep-length approach. Geophysics 83 (3), R99–R123. https://library.seg.org/doi/10.1190/geo2015-0431.1.

Rivera, C., Trinh, P., Bergounioux, E., et al., 2019. Elastic Multiparameter FWI in Sharp Contrast Medium. In: 89th SEG Annual Meeting, pp. 1410–1414. Expanded Abstracts. https://library.seg.org/doi/10.1190/segam2019-3215092.1.

Shin, C., Cha, Y.H., 2008. Waveform inversion in the Laplace domain. Geophys. J. Int. 173, 922–931. https://onlinelibrary.wiley.com/doi/10.1111/j.1365-246X.2008.03768.x.

Shin, C., Cha, Y.H., 2009. Waveform inversion in the Laplace-Fourier domain. Geophys. J. Int. 177, 1067–1079. https://onlinelibrary.wiley.com/doi/10.1111/j.1365-246X.2009.04102.x.

Tang, C., McMechan, G.A., 2018. Multidirectional-vector-based elastic reverse time migration and angle-domain common-image gathers with approximate wavefield decomposition of P- and S- waves. Geophysics 83 (1), S57–S79. https://library.seg.org/doi/10.1190/geo2017-0119.1.

Tarantola, A., 1984. Inversion of seismic reflection data in the acoustic approximation. Geophysics 49 (8), 1259–1266. https://library.seg.org/doi/10.1190/1.1441754.

Vigh, D., Cheng, X., Jiao, K., et al., 2019. Is the salt-related full-waveform inversion sorted out? SEG Annual Meeting 1265–1269. https://library.seg.org/doi/10.1190/segam2019-3215741.1.

Virieux, J., Operto, S., 2009. An overview of full-waveform inversion in exploration geophysics. Geophysics 74 (6), WCC127–WCC152. https://library.seg.org/doi/10.1190/1.3238367.

Wang, T.F., Cheng, J.B., 2017. Elastic full waveform inversion based on mode

decomposition: the approach and mechanism. Geophys. J. Int. 209, 606–622. https://academic.oup.com/gji/article/209/2/606/2966016?searchresult=1.
Wang, Z.Y., Huang, J.P., Liu, D.J., et al., 2019a. 3D variable-grid full-waveform inversion on GPU. Petrol. Sci. 16, 1001–1014. https://link.springer.com/article/10.1007/s12182-019-00368-2.
Wang, G., Yuan, S., Wang, S., 2019b. Retrieving low-wavenumber information in FWI: an efficient solution for cycle skipping. Geosci. Rem. Sens. Lett. IEEE 16 (7), 1125–1129. https://ieeexplore.ieee.org/document/8630819.
Wu, R.S., 1985. Multiple scattering and energy transfer of seismic waves-separation of scattering effect from intrinsic attenuation. I: theoretical modeling. Geophys. J. Int. 82 (1), 57–80. https://onlinelibrary.wiley.com/doi/10.1111/j.1365-246X.1985.tb05128.x.
Wu, R.S., Luo, J.R., Wu, B.Y., 2014. Seismic envelope inversion and modulation signal model. Geophysics 79 (3), WA13–WA24. https://library.seg.org/doi/10.1190/geo2013-0294.1.
Wu, R.S., Zheng, Y.C., 2014. Non-linear partial derivative and its De-Wolf approximation for non-linear seismic inversion. Geophys. J. Int. 196, 1827–1843. https://academic.oup.com/gji/article/196/3/1827/585810?searchresult=1.
Wu, R.S., Chen, G., 2017. New Fréchet Derivative for Envelope Data and Multi-Scale Envelope Inversion, 79th EAGE Annual Meeting, Extended Abstracts. Tu A3 12. https://www.earthdoc.org/content/papers/10.3997/2214-4609.201700833.
Wu, R.S., Chen, G., 2018. Multi-scale Seismic Envelope Inversion Using a Direct Envelope Fréchet Derivative for Strong-Nonlinear Full Waveform Inversion. https://arxiv.org/abs/1808.05275.
Wu, Y., Dorn, O., 2018. A level set method for shape reconstruction in seismic full waveform inversion using a linear elastic model in 2D. J. Phys. Conf. 1311, 012001. https://iopscience.iop.org/article/10.1088/1742-6596/1131/1/012001.
Wu, R.S., 2020. Towards a theoretical background for strong-scattering inversion - direct envelope inversion and gel'fand-levitan-marchenko theory. Commun. Comput. Phys. 28 (1), 41–73. http://www.global-sci.com/intro/article_detail.html?journal=undefined&article_id=16826.
Wu, Z., Liu, Y., Yang, J., 2021. Elastic full-waveform inversion of steeply dipping structures with prismatic waves. Geophysics 86 (4), R413–R431. https://library.seg.org/doi/10.1190/geo2020-0482.1.
Yang, F., Ma, J., 2019. Deep-learning inversion: a next-generation seismic velocity model building method. Geophysics 84 (4), R583–R599. https://library.seg.org/doi/10.1190/geo2018-0249.1.
Yao, G., Wu, D., Wang, S.X., 2020. A review on reflection-waveform inversion. Petrol. Sci. 17, 334–351. https://link.springer.com/article/10.1007/s12182-020-00431-3.
Yong, P., Liao, W.Y., Huang, J.P., et al., 2018. Total variation regularization for seismic waveform inversion using an adaptive primal dual hybrid gradient method. Inverse Probl. 34, 045006. https://iopscience.iop.org/article/10.1088/1361-6420/aaaf8e.
Zhang, Z., Lin, Y., 2020. Data-driven seismic waveform inversion: a study on the robustness and generalization. IEEE Trans. Geosci. Rem. Sens. 58 (10), 6900–6913. https://ieeexplore.ieee.org/document/9044635.
Zhang, P., Han, L., Xu, Z., et al., 2017. Sparse blind deconvolution based low-frequency seismic data reconstruction for multiscale full waveform inversion. J. Appl. Geophys. 139, 91–108. https://www.sciencedirect.com/science/article/abs/pii/S0926985117301635.
Zhang, P., Wu, R.S., Han, L.G., 2018. Source-independent seismic envelope inversion based on the direct envelope Fréchet derivative. Geophysics 83 (6), R581–R595. https://library.seg.org/doi/10.1190/geo2017-0360.1.
Zhang, P., Wu, R.S., Han, L.G., 2019. Seismic envelope inversion based on hybrid scale separation for data with strong noises. Pure Appl. Geophys. 176 (1), 165–188. https://link.springer.com/article/10.1007/s00024-018-2025-4.
Zhang, P., Han, L., Gao, R., et al., 2020. Frequency extension and robust full waveform inversion based on nth power operation. Acta Geophys. Pol. 68, 1317–1333. https://link.springer.com/article/10.1007/s11600-020-00465-6.
Zhang, P., Gao, R., Han, L., et al., 2021. Refraction waves full waveform inversion of deep reflection seismic profiles in the central part of Lhasa Terrane. Tectonophysics 803, 228761. https://www.sciencedirect.com/science/article/abs/pii/S0040195121000457.
Zhang, Q., Zhou, H., Li, Q.Q., et al., 2016. Robust source-independent elastic full-waveform inversion in the time domain. Geophysics 81 (2), R29–R44. https://library.seg.org/doi/10.1190/geo2015-0073.1.
Zhang, Z., Alkhalifah, T., 2019. Local-crosscorrelation elastic full-waveform inversion. Geophysics 84 (6), R897–R908. https://library.seg.org/doi/10.1190/geo2018-0660.1.